

Loading and unloading of a thick-walled cylinder of critical state soils: large strain analysis with applications

Dr. Pei-Zhi **Zhuang**^{1,2,3}, research fellow

Email: p.zhuang@leeds.ac.uk

Professor Hai-Sui **Yu**², FEng

Deputy Vice-Chancellor

E-mail: H.Yu@leeds.ac.uk

Professor Sacha Jon **Mooney**⁴

E-mail: sacha.mooney@nottingham.ac.uk

Dr. Pin-Qiang **Mo**², Associate Research Scientist

Corresponding author

pinqiang.mo@cumt.edu.cn

¹ School of Qilu Transportation, Shandong University, 250002, Jinan, China

² School of Civil Engineering, Faculty of Engineering,
University of Leeds, LS2 9JT Leeds, UK

³ State Key Laboratory for Geomechanics and Deep Underground Engineering China
University of Mining and Technology, 221116, Xuzhou, Jiangsu, China.

⁴ School of Biosciences, University of Nottingham, LE12 5RD Leicestershire, UK

May 2020

Abstract

Thick-walled cylinder (TWC) tests are widely used to obtain soil properties and investigate wellbore instability problems in laboratory-controlled conditions. This paper presents analytical cavity expansion and contraction solutions for modelling undrained TWC tests under three typical loading and unloading programs. Both cylindrical and spherical cavities in critical state soils with a finite radial extent subjected to monotonic loading or unloading under undrained conditions are considered. The solutions are developed in terms of finite strain formulations, and the procedure is applicable to any isotropically hardening materials. Parametric studies show the boundary effect may significantly affect the cavity expansion/contraction response. A limit outer-to-inner diameter ratio of the soil sample exists, beyond which the boundary effect becomes negligible. The limit ratio varies with the cavity geometry, soil stress history (OCR), and cavity deformation level. For undrained TWC tests, a diameter ratio over 20 should normally be adequate to remove the possible boundary effect. Predicted expansion and contraction curves by the new solutions are compared with published data of TWC tests in the literature, and good agreement is shown in each loading/unloading program. This indicates that the boundary effect, which greatly limits the application of conventional cavity expansion/contraction solutions into TWC problems, is successfully captured by the present solutions. The solutions can also serve as valuable benchmark for verifying various numerical methods involving critical state plasticity models.

KEYWORDS: Cavity expansion, Cavity contraction, Thick-walled cylinder tests, Boundary effect, Critical state soil

1 **1 Introduction**

2 Loading and unloading of a thick-walled cylinder (TWC) of soil in a triaxial cell or
3 chamber have been used to investigate the soil behaviour involved in a wide class of
4 geotechnical problems [3,5,27,36]. In laboratory-controlled conditions, three
5 loading/unloading programs are commonly applied in TWC tests, namely internal loading
6 (i.e. increasing the internal pressure), internal unloading (i.e. reducing the internal
7 pressure) and external loading (i.e. increasing the external pressure), while keeping other
8 confining pressures constant [1] (see Fig. 1). The internal loading program (also known
9 as the boundary condition BC1 [27]) is often used to investigate the pressuremeter
10 response [6,26,31,33,35,58]; the internal unloading and external loading programs are
11 common in the study of wellbore instability problems [1,18,24,74].

12 For the purpose of saving energy, time, cost and space during sample preparation and
13 testing and/or improving detectability or traceability of internal soil deformation with
14 non-destructive measurement techniques (e.g. X-ray Computed Tomography), hollow
15 cylinder triaxial apparatuses with outer-to-inner diameter ratios (or chamber diameter to
16 pressuremeter diameter ratio) in a range of 2 to 20 have widely been used in the laboratory
17 [3,5,6,23,26,31,33-36,43,58,60]. It has been reported that significant boundary effects (or
18 container size effect) usually exist in the loading and unloading tests within such small-
19 sized containers, which may lead the measured soil response to be quite different from
20 that in an infinite or 'semi-infinite' soil mass [3,25,29,35,47,49,54,55]. Cavity
21 expansion/contraction theory is a useful theoretical tool for the study of pressuremeter
22 tests and wellbore instability problems [14,18,28,32,42,71]. However, the focus of most
23 previous studies has been on the analysis of a cavity embedded in an infinite soil mass
24 ideally simulating the field conditions [69]. The aforementioned boundary effect is
25 apparently overlooked in these infinite cavity expansion and contraction models.
26 Consequently, they are not suitable for the analysis of pressuremeter and wellbore
27 instability problems in TWC tests as discussed by Juran and BenSaid [34], Silvestri [57],
28 and Abdulhadi [1], among others. To address this problem, this paper presents novel and
29 general solution procedures for undrained cavity expansion and contraction analysis in
30 soils with a finite radial extent under the aforementioned three loading/unloading
31 programs, and a set of analytical/semi-analytical finite strain solutions for several Cam-
32 Clay-type soil models is derived.

33 Before presenting the theoretical analysis, some pioneering studies into quasi-static
34 cavity expansion and contraction behaviour under the considered loading/unloading
35 programs are briefly reviewed. For a cavity expanding and contracting in an infinite soil
36 mass under the internal loading and unloading programs, undrained expansion and
37 contraction solutions in the framework of critical state soil mechanics refer to some
38 pioneering works from Collins and Yu [22], Chen and Abousleiman [15], Vrakas [61],
39 Mo and Yu [40] and Yu and Rowe [73], Vrakas and Anagnostou [62], Chen and
40 Abousleiman [17], Mo and Yu [39], respectively. For brevity, we focus here on reviewing
41 relevant elastic-plastic solutions for the analysis of a cavity embedded in a finite soil mass
42 as below.

43 Existing analytical solutions for the problem of an internally pressurized cavity within
44 a finite soil mass are mainly restricted to elastic-perfectly plastic models such as the
45 Tresca model [30,34,69] and Mohr-Coulomb model [25,48,66,67]. When considering the
46 hardening and softening behaviour of soil, a few semi-analytical drained solutions have
47 also been developed so far. Salgado et al. [53] presented solutions for expansion analysis
48 of a cylindrical cavity in Mohr-Coulomb soils considering non-linear elasticity and
49 variations of friction and dilation angles. The solution was combined with stress rotation
50 analysis to investigate the effects of several types of boundaries to the cone penetration
51 resistance in sand [54]. Adopting an elastic-plastic constitutive model formulated in the
52 critical state framework, Pournaghiazar et al. [48] developed approximate solutions using
53 the similarity technique for both cylindrical and spherical cavities expanded from zero
54 radius subjected to either constant stress or zero displacement at the finite boundary under
55 drained conditions. For the same problem, a more rigorous spherical solution was
56 obtained by Cheng and Yang [19] with the aid of the auxiliary independent variable
57 proposed by Chen and Abousleiman [16]. Cheng et al. [20] further applied the method to
58 the cavity expansion analysis in a finite unsaturated soil mass assuming that the
59 contribution of suction to the effective stress is constant. Lately, Wang et al. [63] derived
60 a solution for a spherical cavity expanding in modified Cam Clay of finite radial extent
61 under undrained conditions. The development of these solutions highly relied on the
62 assumption that the conditions at the elastic-plastic boundary satisfy the plastic and elastic
63 governing equations simultaneously. This requires that the radius of the elastic-plastic
64 boundary must always be smaller than the outer radius of the finite soil medium upon
65 loading, which may valid for the cavity creation or cone penetration problems that were

66 studied in these references. However, this is not generally appropriate for the loading
67 analysis of a hollow cylinder or spherical shell with small outer-to-inter diameter ratios
68 as the entire soil mass may easily yields plastically [49,66,67], in particular for normally
69 consolidated soils. In more general conditions, existing studies into this problem were
70 mainly based on numerical techniques [4,11,35,49].

71 The external loading and internal unloading programs have often been applied in both
72 laboratory tests [1,24,45] and numerical simulations [4,44,74] of TWCs, but a very
73 limited number of analytical solutions were obtained for these cavity contraction
74 problems in a finite soil mass. Durban and Papanastasiou [24] presented semi-analytical
75 solutions for the external compression analysis of a thick-walled cylinder using non-
76 associated Mohr-Coulomb and Drucker-Prager models with arbitrary hardening. Very
77 recently, focusing on the short-term contraction behaviour of soil around shallow tunnels
78 in clay, Zhuang et al. [75] presented a set of undrained cavity contraction solutions for
79 both thick-walled cylinders and spherical shells of Cam clays under the internal unloading
80 program in the companion paper. However, solutions for undrained contraction analysis
81 under the external loading program are not common in the literature to the best knowledge
82 of the authors, particularly for advanced critical state models of soil.

83 In the light of the above discussion, the novelty and importance of the present solutions
84 mainly lie in the following: (a) three typical loading/unloading programs that commonly
85 used in TWC tests are considered, and the associated boundary effect is captured in a
86 rigorous semi-analytical manner; (b) the strain is finite, and the solution procedure
87 applicable for any isotropically hardening materials; and (c) the solution for the unified
88 state parameter model of CASM [68] is able to describe the cavity expansion and
89 contraction behaviour in both clay (including heavily overconsolidated clay) and sand.
90 The paper is structured as follows: Section 2 defines the problem; Section 3 presents the
91 general solution procedure first, which is followed by solutions for several critical state
92 soil models; Section 4 gives results of model validation and parametric studies; Section 5
93 shows comparisons between predicted and measured cavity expansion and contraction
94 curves for TWC tests under three different loading and unloading programs. Finally, some
95 conclusions are drawn.

96 **2 Problem Definition**

97 As depicted in Fig.1, in a hollow cylinder triaxial cell, the soil specimen is subjected to
98 three independently controlled confining stresses: the axial stress (p_a), the uniform radial
99 pressures acting on the inner (p_{in}) and outer (p_{out}) surfaces. The height, the inner and
100 outer diameters of the hollow cylinder specimen are denoted by H , D_i and D_o ,
101 respectively. It has been shown that, with constant axial confining stress, the height of the
102 specimen has minimal effect on the radial expansion or contraction response as long as
103 the ratio of H/D_o is greater than 1.5 [1,3]. In this case, the hollow cylinder
104 loading/unloading tests can be ideally modelled as plane-strain cylindrical cavity
105 expansion/contraction problems. In Fig.1, the inner and outer radii of a soil annulus upon
106 radial loading or unloading are expressed by a and b , respectively, and a_0 and b_0
107 represent their initial values, respectively.

108 It was previously introduced that three typical loading/unloading modes (named as
109 internal loading, internal unloading and external loading) are often applied in TWC tests
110 for investigating pressuremeter and borehole instability problems in the laboratory. In the
111 internal loading or unloading program, the internal radial pressure is increased or
112 decreased monotonically, while keeping the external cell pressure and the axial confining
113 stress constant [3,35,58]. With the external loading program, TWC tests are performed
114 by increasing the external cell pressure, while keeping the internal cavity pressure and the
115 axial stress constant [1,24,74]. In general, the rate of loading/unloading in TWC tests
116 under undrained conditions is much faster than the rates of consolidation and creep of soil
117 [2,4,58], hence the behaviour of soil is considered as rate-independent in this study.

118 The TWC tests subjected to monotonic loading or unloading are transformed into a
119 typical boundary value problem of one-dimensional quasi-static cavity expansion or
120 contraction. It has been shown that the analyses of spherical and long cylindrical cavity
121 problems under uniform stress conditions are quite similar and can be treated
122 simultaneously by introducing a parameter k (k is equal to 1 for a cylindrical cavity and
123 2 for a spherical cavity) [12,22,72,73]. Hence, solutions for the analysis of a thick-wall
124 spherical shell of soil are also derived. The spherical expansion and contraction solutions
125 may offer a chance to model point injection tests (e.g. Au et al. [8]) and cone penetration
126 tests(e.g. Cheng and Yang [19] in small sized calibration chambers and spherical sinkhole
127 formation problems at shallow depths (e.g. Augarde et al. [9]), but this is considered
128 beyond the scope of this paper.

129 For convenience, cylindrical coordinates (r, θ, z) and spherical coordinates (r, θ, φ)
 130 with the origin located at the centre of the cavity are employed for the analysis of thick-
 131 walled cylinder and spherical shell, respectively. The cylindrical cavity
 132 expansion/contraction analyses are performed under plane strain conditions with respect
 133 to the z -axis. Taking compression as positive, the initial stress boundary conditions are
 134 expressed as:

$$135 \quad \sigma_r|_{r=a_0} = p_0 \quad , \quad \sigma_r|_{r=b_0} = p_0 \quad (1 \text{ a,b})$$

136 where σ_r represents the total radial stress. r is the current radial coordinate of a material
 137 element which was initially at r_0 . p_0 is the initial total confining pressure. $p_0 = p'_0 + U_0$,
 138 p'_0 is the initial mean effective stress, and U_0 is the initial ambient pore pressure.

139 The expansion and contraction analyses are performed under undrained conditions.
 140 The surrounding soil is assumed to be homogeneous and isotropic. For convenience, the
 141 mean effective and deviatoric stresses (p', q) below are used for the quasi-static analysis
 142 of the axisymmetric cavity expansion/contraction problem following Collins and Yu [22]
 143 and Yu and Rowe [73].

$$144 \quad p' = \frac{\sigma'_r + k\sigma'_\theta}{1+k} \quad , \quad q = \sigma'_r - \sigma'_\theta \quad (2 \text{ a,b})$$

145 where σ'_r and σ'_θ are the effective radial and circumferential stresses, respectively.

146 The volumetric and shear strains ($\delta; \gamma$) are defined as:

$$147 \quad \delta = \varepsilon_r + k\varepsilon_\theta \quad , \quad \gamma = \varepsilon_r - \varepsilon_\theta \quad (3 \text{ a,b})$$

148 where ε_r and ε_θ are radial and circumferential strains, respectively. It needs to be
 149 pointed out that for the cylindrical case the above definitions for the stress and strain
 150 invariants are slightly different from the usual three-dimensional definitions in critical
 151 state soil models. However, it has been shown (e.g. in references of Sheng et al. [56] and
 152 Chen and Abousleiman [15]) that the error due to these simplifications is negligible for
 153 the analysis of cylindrical cavity problems under an isotropic in-situ stress state which is
 154 of interest in this paper.

155 **3 Undrained cavity expansion/contraction analysis**

156 **3.1 Governing equations**

157 Quasi-static cavity expansion/contraction analysis is mainly concerned with two typical
 158 problems: (a) continuous pressure-displacement curves; and (b) stress and strain
 159 distributions in soil at a given instant. Solutions for them can be obtained by solving a set
 160 of equations of stress equilibrium, deformation compatibility and stress-strain
 161 relationships of soil (as defined below) with given boundary conditions.

162 **(1) Stress equilibrium**

163 Under uniform and monotonic loading or unloading, neglecting body force and
 164 dynamic effect, the stress equilibrium condition along the radial direction can be
 165 expressed in terms of total stresses (Eulerian description) as:

$$166 \quad \sigma_r - \sigma_\theta + \frac{r}{k} \frac{d\sigma_r}{dr} = 0 \quad (4)$$

167 where σ_θ is the total circumferential stress.

168 Since $\sigma_r = p + kq/(k+1)$ and $U = p - p'$ (p : the mean total pressure; U : the pore
 169 pressure), the gradient of U along the radial direction is given as:

$$170 \quad \frac{dU}{dr} = -\frac{dp'}{dr} - \frac{k}{k+1} \frac{dq}{dr} - \frac{k}{r} q \quad (5)$$

171 **(2) Deformation compatibility**

172 For the axisymmetric cavity expansion/contraction problem under undrained
 173 conditions, the constant-volume condition can be expressed as:

$$174 \quad a^{k+1} - a_0^{k+1} = r^{k+1} - r_0^{k+1} = T \quad (6)$$

175 where T is the variable representing the volumetric change of soil at an arbitrary radius.

176 While keeping the external confining pressure constant, internal loading will lead to
 177 outward expansions of the surrounding soil, whereas inward contractions will be caused
 178 by internal unloading. Compressive deformation is taken as positive in this paper. Based
 179 on Eq. (6), the corresponding deformation compatibility equations for these two cases can
 180 be readily obtained [22,73]. Rigorous relations between the finite shear strain and the
 181 radial coordinate without any restriction on the deformation level are given: (a) for a given
 182 particle (i.e. Lagrangian description in Eq. (7)), and (b) at a fixed instant of time (i.e.
 183 Eulerian description in Eq. (8)), respectively, as:

$$184 \quad \gamma = \ln \left[\frac{r_0^{k+1} + T}{r_0^{k+1}} \right] = (k+1) \ln \frac{r}{r_0} \quad (\text{internal loading/unloading}) \quad (7)$$

$$185 \quad \gamma = -\ln \left[1 - \frac{T}{r^{k+1}} \right] \quad (\text{internal loading/unloading}) \quad (8)$$

186 Hence relations between the radial coordinate and shear strain increments: (a) for a
187 given particle, and (b) at a fixed instant of time, respectively, are:

$$188 \quad (k+1) \frac{dr}{r} = d\gamma \quad , \quad (k+1) \frac{dr}{r} = -\frac{d\gamma}{\exp(\gamma) - 1} \quad (\text{internal loading/unloading}) \quad (9 \text{ a, b})$$

189 In the external loading program, the surrounding soil moves inwards (i.e. cavity
190 contraction) with increasing external pressures. The soil movement is similar to that
191 which occurred in the internal unloading program, but the soil deforms under
192 compression. Therefore, new relations between the finite shear strain and the radial co-
193 ordinate are constructed in Eqs. (10) and (11), which are: (a) for a given particle, and (b)
194 at a fixed instant of time, respectively.

$$195 \quad \gamma = -\ln \left[\frac{r_0^{k+1} + T}{r_0^{k+1}} \right] = -(k+1) \ln \frac{r}{r_0} \quad (\text{external loading}) \quad (10)$$

$$196 \quad \gamma = \ln \left[1 - \frac{T}{r^{k+1}} \right] \quad (\text{external loading}) \quad (11)$$

197 and the incremental expressions of these relations become:

$$198 \quad (k+1) \frac{dr}{r} = -d\gamma \quad , \quad (k+1) \frac{dr}{r} = -\frac{d\gamma}{\exp(-\gamma) - 1} \quad (\text{external loading}) \quad (12 \text{ a,b})$$

199 (3) Stress-strain relationships

200 The stress-strain relationships are conveniently defined in general forms appropriate
201 for a wide class of two-invariant critical state soil models in this subsection. Before
202 entering plastic, soil behaviour is purely elastic. The elastic constitutive law is expressed
203 in rate forms as:

$$204 \quad \dot{\delta}^e = \frac{\dot{p}'}{K(p', \nu)} \quad , \quad \dot{\gamma}^e = \frac{\dot{q}}{2G(p', \nu)} \quad (13 \text{ a,b})$$

205 where $\dot{\delta}^e$ and $\dot{\gamma}^e$ represent the elastic volumetric and shear strain rates, respectively.

206 $K(p', \nu)$ and $G(p', \nu)$ are the instantaneous bulk and shear moduli, which are pressure-

207 dependent (e.g. Eq.14). v is the specific volume. The symbol $(\dot{\quad})$ denotes the material
 208 time derivative associated with a given material particle; $(\dot{\quad})$ denotes the local time
 209 derivate, evaluated at a fixed position r .

210 The hypoelastic model that commonly adopted in Cam-Clay-type models (e.g. Table
 211 1) can be recovered by combining Eqs. (13) and (14).

$$212 \quad K(p', v) = vp' / \kappa \quad , \quad G(p', v) = \varpi \frac{vp'}{\kappa} \quad (14 \text{ a,b})$$

213 where $\varpi = 0.5[(1+k)(1-2\mu)]/[1+(k-1)\mu]$, and μ denotes Poisson's ratio of soil. κ
 214 denotes the slope of the swelling line in the $v - \ln p'$ space.

215 The loading and unloading programs are treated in a single analysis by introducing a
 216 parameter ζ (i.e. $\zeta = 1$ for internal and external loading; $\zeta = -1$ for internal unloading)
 217 in this paper. Then the yield function and the plastic flow rule that used to describe the
 218 plastic behaviour of soil (e.g. Table 1) are written in a general form as:

$$219 \quad q = f(p', p'_y) \quad , \quad \frac{\dot{\delta}^p}{\dot{\gamma}^p} = \frac{\partial g / \partial p'}{\partial g / \partial q} = D(\eta) \quad (15\text{a,b})$$

220 where g is the plastic potential; $D(\eta)$ represents the stress–dilatancy function;
 221 $\eta = \zeta q / p'$, is the stress ratio. p'_y denotes the preconsolidation pressure, which controls
 222 the size of the yield surface as a hardening parameter. In usual Cam-Clay type soil models
 223 [50,51,68], hardening is attributed solely to accumulated plastic volumetric strains, and
 224 the volumetric hardening rule of Eq.(16) is usually adopted.

$$225 \quad d\delta^p = \frac{(\lambda - \kappa)}{v} \frac{dp'_y}{p'_y} \quad (16)$$

226 where λ denotes the slope of the normal consolidation line (NCL) in the $v - \ln p'$ space.

227 Table 1 Critical state constitutive models considered in the present study.

| Model | Yield function | Stress–dilatancy function $D(\eta)^*$ |
|---------------------------|---|---|
| Original Cam-Clay [51] | $q = \zeta Mp' \ln(p'_y / p')$ | $D(\eta) = \zeta \frac{k}{(k+1)} (M - \eta)$ |
| Modified Cam-Clay [50] | $q = \zeta Mp' \sqrt{p'_y / p' - 1}$ | $D(\eta) = \zeta \frac{k}{(k+1)} \frac{M^2 - \eta^2}{2\eta}$ |
| CASM [68] | $q = \zeta Mp' \left[-\frac{\ln(p' / p'_y)}{\ln r^*} \right]^{1/n} \S$ | $D(\eta) = \zeta \frac{k}{(k+1)} \frac{9(M - \eta)}{(9 + 3M - 2M\eta)}$ |

228 * Note that the conjugate shear strain to the shear stress of Eq. (2b) is in the form of
 229 $\varepsilon_q = k\gamma / (k + 1)$. Accordingly, expressions of $D(\eta)$ are modified by definition.

230 § n and r^* are the stress-state coefficient and the spacing ratio, respectively. r^* controls
 231 the intersection position of the the critical state line (CSL) and the yield surface; n
 232 defines the shape of the yield surface (see Fig.2) in CASM [68].

233 The critical state is defined by the following two equations [52].

$$234 \quad v = \Gamma - \lambda \ln p' \quad (17)$$

$$235 \quad q = \zeta M p' \quad (18)$$

236 where Γ is the value of v on the CSL at $p'=1\text{kPa}$. M is the slope of the CSL in the p'
 237 - q space, which can be expressed as $M = [2(k + 1)\sin \varphi_{cs}] / [(k + 1) - (k - 1)\sin \varphi_{cs}]$ for
 238 the present problem with Eq. (2). φ_{cs} is the critical state friction angle of soil. It has been
 239 shown that φ_{cs} measured in plane strain tests is up to 10-20% larger than that in triaxial
 240 compression tests (φ_{tc}) due to the shear mode effect (or intermediate effective stress
 241 effect) [13,65]. To account for this effect in the analysis, it is assumed that φ_{cs} equals 1.1-
 242 1.2 times of φ_{tc} for the plane strain conditions ($k=1$) and $\varphi_{cs} = \varphi_{tc}$ for the spherical
 243 symmetric conditions ($k=2$) [20].

244 **3.2 Analytical effective stress analysis under undrained loading and unloading**

245 The above stress-strain relationships define that one soil element may successively enter
 246 three stress states (including purely elastic state, elastic-plastic state, and critical state)
 247 upon monotonic loading or unloading. Solutions for each state are derived as follows.

248 **(1) Purely elastic state**

249 According to the constant-volume condition and Eq. (13a), the mean effective stress
 250 remains constant and equals its initial value p'_0 at the purely elastic state. Therefore, the
 251 bulk and shear moduli also remain constant and equal to their initial values K_0 and G_0
 252 respectively. The elastic shear stress q^e can be obtained by integrating Eq. (13b) along a
 253 particle path as:

$$254 \quad q^e = 2G_0\gamma \quad (19)$$

255 Then the effective radial and circumferential stresses ($\sigma'_r{}^e$ and $\sigma'_\theta{}^e$) are given as:

$$256 \quad \sigma_r'^e = p'_0 + \frac{k}{k+1} q^e, \quad \sigma_\theta'^e = p'_0 - \frac{1}{k+1} q^e \quad (20)$$

257 (2) Elastic-plastic state

258 The soil yields plastically when the shear stress invariant reaches the yield value of q_{ep}
 259 , which will depend upon the particular yield criterion. According to Eqs. (7) (or (10))
 260 and (19), plastic deformation occurs first at the inner wall of the cavity upon loading or
 261 unloading, and the corresponding limit elastic shear strain equals:

$$262 \quad \gamma_{ep} = \frac{q_{ep}}{2G_0} \quad (21)$$

263 The plastic zone propagates outwards with subsequent loading or unloading. From Eqs.
 264 (8) (or (11)) and (21), the current and initial radii of the elastic-plastic boundary (c and
 265 c_0 , respectively) at the instant of the cavity with a radius of a under different
 266 loading/unloading programs can be expressed, respectively, as:

$$267 \quad \left(\frac{c}{a}\right)^{k+1} = \frac{(a_0/a)^{k+1} - 1}{\exp(-\gamma_{ep}) - 1}, \quad c_0 = (c^{k+1} + T)^{\frac{1}{k+1}} \quad (\text{internal loading/unloading}) \quad (22a,b)$$

$$268 \quad \left(\frac{c}{a}\right)^{k+1} = \frac{(a_0/a)^{k+1} - 1}{\exp(\gamma_{ep}) - 1}, \quad c_0 = (c^{k+1} + T)^{\frac{1}{k+1}} \quad (\text{external loading}) \quad (23a,b)$$

269 As $\dot{\delta}^e + \dot{\delta}^p = 0$ under undrained conditions, integrating Eqs. (13a) and (16) gives:

$$270 \quad \kappa \ln\left(\frac{p'}{p'_0}\right) + (\lambda - \kappa) \ln\left(\frac{p'_y}{p'_{y0}}\right) = 0 \quad (24)$$

271 Eq. (24) defines a relationship between the hardening parameter p'_y and the mean
 272 effective stress, by which the functions of $f(p', p'_y)$ and $D(\eta)$ in Eqs. (15 a,b) can be
 273 explicitly converted into functions in terms of p' solely (e.g. Table 2). Then the total
 274 elastic-plastic shear strain rate $\dot{\gamma}$ can be expressed into Eq. (25) based on the constant-
 275 volume condition and Eqs. (13)-(16).

$$276 \quad \dot{\gamma} = \dot{\gamma}^e + \dot{\gamma}^p = L(p') \dot{p}' \quad (25)$$

277 where

$$L(p') = \frac{q'(p')}{2G(p')} - \frac{1}{K(p')D(\eta)} \quad (26)$$

Integrating Eq.(25) in terms of p' along a particle path starting from the initial yield time, at which $p' = p'_0$ and $q = q_{ep}$, gives an expression of γ as:

$$\gamma = \gamma_{ep} + I(p') - I(p'_0) \quad (27)$$

where

$$I(p') = \int^{p'} L(p') dp' \quad (28)$$

Note that Eqs. (24)-(28) suit for any case of stress-controlled proportional loading or unloading under undrained conditions [46], which certainly includes the loading/unloading programs considered in this study.

(3) Critical state

Under undrained conditions, the specific volume of soil remain unchanged. Therefore, once the soil has reached the critical state, the mean effective stress and shear stress remain constant (i.e. p'_{cs} and q_{cs} , respectively) as defined by in Eqs. (17) and (18), values of which will depend upon the particular yield criterion.

(4) Solution procedure for effective stresses

Taking the CASM model [68] as an example, here the procedure to derive the functions of $I(p')$ and $L(p')$ is further detailed. Based on Eq. (24), the yield function of CASM (see Table 1) is converted into Eq. (29) in terms of p' , which is required for obtaining an explicit expression of $L(p')$.

$$q(p') = \zeta Mp [A_1 + A_2 \ln p']^{1/n} \quad (29)$$

in which

$$A_1 = \frac{\ln R_0 + \Lambda^{-1} \ln p'_0}{\ln r^*}, \quad A_2 = -\frac{\Lambda^{-1}}{\ln r^*}, \quad \text{and} \quad \Lambda = \frac{\lambda - \kappa}{\lambda}. \quad (30 \text{ a,b,c})$$

where R_0 is the isotropic over-consolidation ratio, defines as p'_{y0} / p'_0 . p'_{y0} is the initial value of p'_y . R_0 is different from the usual one-dimensional definition of the over-consolidation ratio (i.e. OCR), and relationships between R_0 and OCR refer to the

303 references of Wood [64], Yu and Collins [71] and Chang et al. [13]. Eq. (29) can recover
 304 the yield surface of the original Cam-Clay model exactly by choosing $n=1$ and $r^*=2.718$
 305 (e.g. Fig.2a); the ‘wet’ side of the modified Cam-Clay model can be approximated by
 306 choosing $r^*=2$ in conjunction with a suitable value of n (e.g. Fig.2b).

307 With the given constitutive equations of CASM and Eq. (26), the function of $L(p')$ is
 308 obtained as:

$$309 \quad L(p') = \zeta \frac{\kappa}{vp'} \left\{ \frac{M}{2\varpi} \left[(A_1 + A_2 \ln p')^{1/n} + \frac{A_2}{n} (A_1 + A_2 \ln p')^{1/n-1} \right] - \frac{(k+1)(9+3M-2M\eta)}{k \cdot 9(M-\eta)} \right\} \quad (31)$$

310 Then integrating Eq. (31) in terms of p' along the stress history of a particle gives:

$$311 \quad I(p') = \zeta \frac{\kappa M}{2\varpi v} \left[\frac{n}{(1+n)A_2} (A_1 + A_2 \ln p')^{\frac{1}{n}+1} + (A_1 + A_2 \ln p')^{\frac{1}{n}} \right] \quad (32)$$

$$- \zeta \frac{\kappa n(m+1)}{9vA_2 M^n m} \left[\frac{2M}{n} \eta^n + (9+3M-2M^2) \int \frac{\eta^{n-1}}{M-\eta} d\eta \right]$$

312 in which

$$313 \quad \int \frac{\eta^{n-1}}{M-\eta} d\eta = \frac{\eta^n \left[n {}_2F_1(1, n+1; n+2; \eta/M) + M(n+1) \right]}{n(n+1)M^2} \quad (33)$$

314 where ${}_2F_1(1, n+1; n+2; \eta/M)$ is the Gaussian hypergeometric function in terms of
 315 η/M .

316 With $p' = p'_0$, Eq. (29) gives the elastic limit of the shear stress in Eq. (34).

$$317 \quad q_{ep} = \zeta \left(\frac{\ln R_0}{\ln r^*} \right)^{\frac{1}{n}} M p'_0 \quad (34)$$

318 Then by substituting Eq. (34) into Eq. (21), the elastic limit of the shear strain (γ_{ep})
 319 required for the determination of the finite shear strain in Eq.(27) is known.

320 Similarly, solutions of $I(p')$ and $L(p')$ for the widely used original and modified
 321 Cam-Clay models are also derived as given in Table 2. The above procedure is applicable
 322 for any constitutive model in the form of that defined in the last subsection.

323 Table 2 Solutions of $I(p')$ and $L(p')$ for original and modified Cam-Clay models.

| Model | Solutions |
|-------|-----------|
|-------|-----------|

| | |
|----------------------|---|
| | $q(p') = -\zeta Mp' \left(\frac{1}{\Lambda} \ln \frac{p'}{p'_0} - \ln R_0 \right), \quad q_{ep} = \zeta Mp'_0 \ln R_0$ |
| Original Cam-Clay | $L(p') = -\zeta \left\{ M \left(\frac{1}{\Lambda} + \frac{1}{\Lambda} \ln \frac{p'}{p'_0} - \ln R_0 \right) \frac{\kappa}{2\sigma v p'} + \frac{(k+1)}{k} \frac{\kappa}{v p' (M - \eta)} \right\}$ $I(p') = -\zeta \left\{ \frac{\kappa M}{2\sigma v} \left[\frac{1}{2\Lambda} (\ln p')^2 + \left(\frac{1}{\Lambda} - \frac{1}{\Lambda} \ln p'_0 - \ln R_0 \right) \ln p' \right] + \frac{(k+1)}{k} \frac{\kappa \Lambda}{v M} \ln (M - \eta) \right\}$ |
| Modified Cam-Clay | $q(p') = \zeta Mp' \sqrt{R_0 (p' / p'_0)^{-1/\Lambda} - 1}, \quad q_{ep} = \zeta Mp'_0 \sqrt{R_0 - 1}$ $L(p') = \zeta \left\{ \frac{\kappa M}{2\sigma v p'} \frac{\left(1 - \frac{1}{2\Lambda}\right) \left(\left(\frac{\eta}{M}\right)^2 + 1\right) - 1}{\eta / M} - \frac{(k+1)}{k} \frac{\kappa}{v p'} \frac{2\eta}{(M^2 - \eta^2)} \right\}$ $I(p') = \zeta \left\{ \frac{\kappa}{2\sigma v} \left[(1 - 2\Lambda)\eta + 2M\Lambda \tan^{-1} \frac{\eta}{M} \right] + \frac{2(k+1)}{k} \frac{\kappa \Lambda}{v M} \left[\tanh^{-1} \frac{\eta}{M} - \tan^{-1} \frac{\eta}{M} \right] \right\}$ |

324 Once the soil has reached the critical state, the mean effective stress and shear stress
325 remain constant (i.e. p'_{cs} and q_{cs} , respectively) under undrained conditions. For the
326 constitutive models listed in Table 1, p'_{cs} and q_{cs} can be expressed as:

$$327 \quad p'_{cs} = p'_0 \left(\frac{R_0}{r^*} \right)^\Lambda = \exp\left(\frac{\Gamma - v}{\lambda}\right), \quad q_{cs} = \zeta Mp'_{cs} \quad (35 \text{ a,b})$$

328 where $r^* = 2.718$ and $r^* = 2$ for the original and modified Cam clays, respectively.

329 In the above, the shear strain was expressed in two ways by means of strain
330 compatibility analyses and integrations of the stress-strain relationships, respectively.
331 Based on them, the effective stresses in the soil can be readily related to the kinematic
332 process of cavity expansion/contraction. In summary, (a) during purely elastic loading or
333 unloading, p' remains constant as p'_0 , and q can be obtained by Eq.(19) in conjunction
334 with the compatibility relations (i.e. Eqs. (7), (8), (10) and (11)); (b) in the elastic-plastic
335 state, continuous changes of the effective stresses in a given soil element upon loading or
336 unloading can be determined by equalling Eq. (27) with Eq. (7) (or Eq. (10)), and
337 distributions of the effective stresses along the radial coordinate at a fixed instant can be
338 determined by equalling Eq. (27) with Eq. (8) (or Eq. (11)); (c) in the critical state, both
339 p' and q remain constants as defined in Eq. (35).

340 3.3 Calculation of excess pore pressures

341 The excess pore pressure (ΔU) at a given instant can be determined by integrating Eq.
 342 (5) along the radial direction. Although all soil particles go through the same effective
 343 stress path, the total stress path of each element varies along the radial direction due to
 344 the difference in the total pressure between the inner and outer boundaries of the finite
 345 soil mass [35]. This is different to the self-similar cavity expansion or contraction problem
 346 in an infinite soil mass and makes the solution procedure for obtaining ΔU become more
 347 complicated. A general solution procedure for this typical non-self-similar boundary
 348 value problem is developed as follows.

349 (1) Solutions for a cavity under loading or unloading

350 In the internal loading or unloading program, the total radial pressure at the outer
 351 boundary (i.e. $r = b$) is kept constant. With Eq. (9b), integrating Eq. (5) from $r = b$
 352 gives:

$$353 \quad \Delta U|_r = \Delta U|_b - (p'_r - p'_b) - \frac{k}{k+1}(q|_r - q_b) + \frac{k}{k+1} \int_{\gamma_b}^{\gamma} \frac{q d\gamma}{\exp(\gamma) - 1} \quad (36)$$

354 where $\Delta U|_r$, p'_r and $q|_r$ are excess pore pressure, mean effective stress and shear stress
 355 at an arbitrary radius of r . γ_b and $\Delta U|_b$ are the shear strain and the excess pore pressure
 356 at $r = b$, respectively.

357 It is clear that $\Delta U|_r$ depends on the effective stress states of soil at both $r = b$ and the
 358 position of concern. According to the stress state at both positions, it is found that six
 359 phases possibly occur. To facilitate the calculation of $\Delta U|_r$, Eq. (36) can be simplified
 360 into different forms at different phases as follows.

361 (a) Purely elastic phase (elastic at both $r = b$ and $r = a$)

362 While the entire soil mass stays at the purely elastic state, the mean effective stresses
 363 in the whole field remain constant and equal p'_0 . The shear stresses are known with Eq.
 364 (19). Hence, by simplifying Eq. (36), a closed-form solution for $\Delta U|_r$ in the elastic region
 365 is obtained as:

$$366 \quad \Delta U|_r = -\frac{k}{k+1} q + \frac{2G_0 k}{k+1} \int_{\gamma_b}^{\gamma} \frac{\gamma d\gamma}{\exp(\gamma) - 1} \quad (37)$$

367 in which

$$368 \quad \int \frac{\gamma d\gamma}{\exp(\gamma)-1} \doteq -\sum_{i=1}^{\infty} \frac{[1-\exp(\gamma)]^i}{i^2} - \frac{\gamma^2}{2} \quad (38)$$

369 (b) Elastic-plastic phase (elastic at $r = b$ and plastic at $r = a$)

370 Upon further loading or unloading, soil particles enter the plastic state first at the inner
 371 cavity wall. Subsequently, the plastic region propagates outwards, the radius of which
 372 can be determined by Eq. (22). In the elastic-plastic phase that the soil at $r = b$ remains
 373 elastic while the soil at $r = a$ yields plastically already, $\Delta U|_r$ in the outside elastic region
 374 can be calculated by Eq. (37). Thus the excess pore pressure at the elastic-plastic
 375 boundary (i.e. $\Delta U|_{r=c}$) is obtained as the shear strain therein (i.e. γ_{ep}) is known from Eq.
 376 (21). Then the excess pore pressure within the inside plastic region is obtained from Eqs.
 377 (15a), (27) and (36) as:

$$378 \quad \Delta U|_r = \Delta U|_{r=c} - (p' - p'_0) - \frac{k}{k+1} [q - q_{ep} - J_{partial}] \quad (39)$$

379 in which

$$380 \quad J_{partial} = \int_{\gamma_{ep}}^{\gamma} \frac{q d\gamma}{\exp(\gamma)-1} = \int_{p'_0}^{p'} \frac{qL(p') dp'}{\exp(\gamma)-1} \quad (40)$$

381 With further loading or unloading, two phases may appear according to the stress states
 382 at $r = b$ and at $r = a$. One is that the soil at $r = a$ enters the critical state while the soil
 383 at $r = b$ still stays as elastic. The other is that the soil at $r = b$ yield plastically before the
 384 soil at $r = a$ enters the critical state. The sequence of occurrence of these two phases
 385 mainly depends on the ratio of b_0 / a_0 and the stress history (e.g. R_0). Therefore, solutions
 386 for them are given as follows in no particular order.

387 (c) Elastic-critical-state phase (elastic at $r = b$ and critical state at $r = a$)

388 In this phase, elastic, plastic and critical state regions exist simultaneously within the
 389 surrounding soil from the outside in. $\Delta U|_r$ in the outside two regions can be calculated
 390 with the procedure for the analysis of the elastic-plastic phase. Hence, the value at the
 391 plastic-critical-state boundary $r = r_{cs}$ (i.e. $\Delta U|_{r=r_{cs}}$) can be obtained from Eq. (39) with
 392 inputs of the critical state effective stresses (i.e. p'_{cs} and q_{cs} in Eq. (35 a,b). Then $\Delta U|_r$
 393 within the critical state region (i.e. $a \leq r \leq r_{cs}$) can be obtained from Eq. (36) as:

394
$$\Delta U|_r = \Delta U|_{r=r_{cs}} + \frac{kq_{cs}}{k+1} \ln \left[\frac{\exp(-\gamma) - 1}{\exp(-\gamma_{cs}) - 1} \right] \quad (41)$$

395 where γ_{cs} is the shear strain at $r = r_{cs}$.

396 (d) Fully plastic phase (plastic at both $r = b$ and $r = a$)

397 In this case, Eq. (36) goes to:

398
$$\Delta U|_r = \Delta U|_{r=b} - (p' - p'_b) - \frac{k}{k+1} [q - q_b - J_{full}] \quad (42)$$

399 in which

400
$$J_{full} = \int_{\gamma_b}^{\gamma} \frac{qd\gamma}{\exp(\gamma) - 1} = \int_{p'_b}^{p'} \frac{qL(p')dp'}{\exp(\gamma) - 1} \quad (43)$$

401 At a known expansion/contraction instant, γ_b can be determined by Eqs. (6) and (7)

402 as:

403
$$\gamma_b = (k+1) \ln \left[\left(b_0^{k+1} + T \right)^{1/(k+1)} / b_0 \right] \quad (44)$$

404 The mean effective stress at $r = b$ (i.e. p'_b) in this phase can thus be back-calculated

405 by equalling Eqs. (27) and (44), and the shear stress at $r = b$ (i.e. q_b) is then known from

406 the yield function. Finally, as the external radial total pressure is kept constant, $\Delta U|_{r=b}$ is

407 obtained as:

408
$$\Delta U|_{r=b} = p'_0 - [p'_b + kq_b / (k+1)] \quad (45)$$

409 (e) Plastic-critical-state phase (plastic at $r = b$ and critical state at $r = a$)

410 Following the above phases, the soil at $r = a$ may enter the critical state upon further

411 loading or unloading, which results in two stress regions within the surrounding soil,

412 namely plastic and critical state regions from the outside in. Similarly, $\Delta U|_r$ within the

413 outside plastic region can be determined taking the previous procedure for the fully-

414 plastic phase (i.e. Eq. (42)); ΔU within the critical state region in this phase can be

415 computed with Eqs. (41) and (42).

416 (f) Fully critical-state phase of expansions

417 If the entire soil mass enters the critical state, the excess pore pressures can be readily

418 obtained from Eq.(36) as:

$$419 \quad \Delta U = \Delta U|_{r=b}^{cs} + \frac{kq_{cs}}{k+1} \ln \left[\frac{\exp(-\gamma) - 1}{\exp(-\gamma_b) - 1} \right] \quad (46)$$

420 where $\Delta U|_{r=b}^{cs} = p'_0 - [p'_{cs} + kq_{cs} / (k+1)]$.

421 (2) Solutions for a cavity under external loading

422 In the external loading program, the internal cavity pressure is kept constant. In this
 423 case, to determine the excess pore pressure $\Delta U|_r$ within the surrounding soil, Eq. (5)
 424 should be integrated from the inner cavity wall (i.e. $r = a$). With the use of Eq. (12b), the
 425 integration of Eq. (5) gives:

$$426 \quad \Delta U|_r = \Delta U|_a - (p'|_r - p'_a) - \frac{k}{k+1} (q|_r - q_a) + \frac{k}{k+1} \int_{\gamma_a}^{\gamma} \frac{qd\gamma}{\exp(-\gamma) - 1} \quad (47)$$

427 where $\Delta U|_a$, p'_a and q_a are the excess pore pressure, the mean effective stress and the
 428 plastic shear stress at $r = a$, respectively. γ_a is the shear strain at $r = a$.

429 According to Eqs. (6) and (47), $\Delta U|_r$ under the external loading program can be
 430 obtained in a similar procedure as that developed for the other two programs, although
 431 the paths of integration are opposite. The solution procedure is presented briefly as follow.

432 (a) Purely elastic phase (elastic at both $r = b$ and $r = a$)

433 By simplifying Eq. (47), $\Delta U|_r$ in the elastic region can be rewritten as:

$$434 \quad \Delta U|_r = -\frac{k}{k+1} q + \frac{2G_0k}{k+1} \int_{\gamma_a}^{\gamma} \frac{\gamma d\gamma}{\exp(-\gamma) - 1} \quad (48)$$

435 in which

$$436 \quad \int \frac{\gamma d\gamma}{\exp(\gamma) - 1} \doteq \sum_{i=1}^{\infty} \frac{[1 - \exp(\gamma)]^i}{i^2} \quad (49)$$

437 At a given instant, γ_a can be calculated from Eqs. (6) and (10) as:

$$438 \quad \gamma_a = -(k+1) \ln \left[\left(a_0^{k+1} + T \right)^{1/(k+1)} / a_0 \right] \quad (50)$$

439 (b) Elastic-plastic phase (elastic at $r = b$ and plastic at $r = a$)

440 The current and initial radii of the elastic-plastic boundary were given in Eqs. (23a,b).

441 $\Delta U|_r$ within the inside plastic region (i.e. $a \leq r \leq c$) can be expressed as:

$$442 \quad \Delta U|_r = \Delta U|_{r=a} - (p' - p'_a) - \frac{k}{k+1} [q - q_a - J_{partial}] \quad (51)$$

443 in which

$$444 \quad J_{partial} = \int_{\gamma_a}^{\gamma} \frac{q d\gamma}{\exp(-\gamma) - 1} = \int_{p'_a}^{p'} \frac{qL(p') dp'}{\exp(-\gamma) - 1} \quad (52)$$

445 The mean effective stress p'_a can be back-calculated by equalling Eqs. (27) and (50),

446 and the plastic shear stress q_a is then known from the yield function. As the internal radial

447 pressure is kept constant, $\Delta U|_{r=a}$ equals:

$$448 \quad \Delta U|_{r=a} = p'_0 - [p'_a + kq_a / (k+1)] \quad (53)$$

449 The excess pore pressure at the elastic-plastic boundary ($\Delta U|_{r=c}$) can then be computed

450 by inputting $p' = p'_0$ and $q = q_{ep}$ into Eq. (51). Substituting the above values into Eq.

451 (47), $\Delta U|_r$ within the outside elastic region is obtained as:

$$452 \quad \Delta U|_r = \Delta U|_{r=c} - \frac{k}{k+1} (2G_0\gamma - q_{ep}) + \frac{2kG_0}{k+1} \int_{\gamma_c}^{\gamma} \frac{\gamma d\gamma}{\exp(-\gamma) - 1} \quad (54)$$

453 (c) Elastic-critical-state phase (elastic at $r = b$ and critical state at $r = a$)

454 At this phase, $\Delta U|_r$ in the inside critical state region (i.e. $a \leq r \leq r_{cs}$) can be obtained

455 as:

$$456 \quad \Delta U|_r = \Delta U|_{r=a} + \frac{kq_{cs}}{k+1} \ln \left[\frac{\exp(\gamma_a) - 1}{\exp(\gamma) - 1} \right] \quad (55)$$

457 With Eq. (55), the excess pore pressure at $r = r_{cs}$ (i.e. $\Delta U|_{r=r_{cs}}$) can be determined with

458 inputs of p'_{cs} and q_{cs} . Taking the stress conditions at $r = r_{cs}$ as the initial values, $\Delta U|_r$

459 in the outside two regions can be calculated taking the above procedure for the analysis

460 of the elastic-plastic phase.

461 (d) Fully plastic phase (plastic at both $r = b$ and $r = a$)

462 In this phase, Eq. (47) can be simplified to be:

$$463 \quad \Delta U|_r = \Delta U|_{r=a} - (p' - p'_a) - \frac{k}{k+1} [q - q_a - J_{full}] \quad (56)$$

464 in which

$$465 \quad J_{full} = \int_{\gamma_a}^{\gamma} \frac{q d\gamma}{\exp(-\gamma) - 1} = \int_{p'_a}^{p'} \frac{qL(p') dp'}{\exp(-\gamma) - 1} \quad (57)$$

466 Stresses at $r = a$ can be obtained with the same method that was just introduced above.

467 (e) Plastic-critical-state phase (plastic at $r = b$ and critical state at $r = a$)

468 At this phase, $\Delta U|_r$ within the inside critical state region can be computed using Eq.

469 (55); $\Delta U|_r$ within the outside plastic region can be determined from Eq. (56) with initial

470 values of stresses conditions at $r = r_{cs}$ instead of those at $r = a$.

471 (f) Fully critical-state phase

472 When the entire soil enters the critical state, Eq. (47) can be simplified as:

$$473 \quad \Delta U|_r = \Delta U|_{r=a}^{cs} + \frac{kq_{cs}}{k+1} \ln \left[\frac{\exp(\gamma_a) - 1}{\exp(\gamma) - 1} \right] \quad (58)$$

474 where $\Delta U|_{r=a}^{cs} = p'_0 - [p'_{cs} + kq_{cs} / (k+1)]$.

475 **4 Solution validation and parametric analysis**

476 This section presents some selected results of cavity expansion and contraction curves

477 under different loading/unloading programs. The following results were calculated with

478 the critical state parameters relevant to London Clay ($\Gamma = 2.759$, $\lambda = 0.161$, $\kappa = 0.062$,

479 $\varphi_{cs} = 22.75^\circ$ [22]), $\nu = 2.0$ and $\mu = 0.3$. All the results are normalised by the undrained

480 shear strength s_u , which can be obtained with $q_{cs} = 2s_u$ as:

$$481 \quad s_u = 0.5Mp'_0 \left(R_0 / r^* \right)^\Lambda \quad (59)$$

482 **4.1 Cavity response under internal loading**

483 Solutions for cavity expansion in an infinite soil mass under internal loading have been

484 developed by Collins and Yu [22] and Mo and Yu [40] for the (original and modified)

485 Cam-Clay and CASM models, respectively. While taking the surrounding soil as infinite

486 (i.e. setting $a_0 / b_0 \propto 0$), the present solutions can reduce exactly to their solutions.

487 Taking the solution for the modified Cam-Clay model as an example, selected results for
488 clay samples with different values of R_0 and b_0/a_0 are compared in Figs. 3-5 to show their
489 effects to the cavity expansion response and associated stress distributions.

490 Fig. 3 shows that the present solution gave virtually the same results as Collins and Yu
491 [22] while considering an infinite soil mass. For a finite soil mass under internal loading,
492 the ratio of b_0/a_0 may greatly influence the cavity pressure-expansion response. For
493 example, with an expansion level up to $a/a_0=4$, three typical pressure-expansion
494 responses are shown in Fig. 3, including: (a) In an infinite soil mass, a limit cavity
495 pressure is reached (typically at around $a/a_0=2$), and this value remains almost constant
496 during afterwards expansions. (b) For a cavity embedded in an intermediate-thick soil
497 mass, a maximum cavity pressure close to the aforementioned limit pressure is reached
498 upon loading. However, the cavity pressure drops with afterwards expansions when the
499 effect of the constant stresses at the outer boundary prevails. (c) For a thin hollow cylinder
500 or spherical shell, the maximum cavity pressure that can be reached is much smaller than
501 the limit pressure, and the cavity pressure drops after a local peak when the outside
502 boundary effect is activated and eventually gets close to the outside radial confining
503 pressure at sufficiently large deformations. Overall, the maximum cavity pressure that the
504 surrounding soil can sustain may decrease significantly with a decreasing value of b_0/a_0 .
505 A limit value of b_0/a_0 exists, beyond which the cavity expansion response is immune from
506 the outer boundary effect. The limit ratio of b_0/a_0 decreases with increases of the over-
507 consolidation ratio, and the limit ratio for a spherical cavity is generally smaller than that
508 for a cylindrical cavity.

509 The observed reduction in the total cavity pressure during expansion is further
510 explained by plotting results of stress distributions in the soil (Figs. 4 and 5) and stress
511 paths of soil at the inner wall (Fig. 6) for typical values of b_0/a_0 and the over-consolidation
512 ratio. The results were calculated with expansions up to $a/a_0=4$. Note the peak and
513 ultimate points in Fig. 6(c) and 6(d) correspond to the points at which the peak and
514 ultimate values of the internal cavity pressure were reached in Fig. 3, respectively. For
515 the cylindrical case, increments of the out-of-plane stress were calculated using
516 $\Delta\sigma'_z = \nu(\Delta\sigma'_r + \Delta\sigma'_\theta)$ according to the plane strain assumption [72]. It was shown that the
517 outer boundary effect may alter the total stress path of a soil particle but applies no
518 influence on the effective stress path, which is consistent with that has been observed by
519 Juran and Mahmoodzadegan [35] in undrained TWC tests. At a given deformation level,

520 Figs. 4-6 show that the excess pore pressures generated throughout the hollow cylinder
 521 or spherical shell are typically smaller than that generated at the same radii in the
 522 corresponding case of an infinite soil mass when the outer boundary effect applies, and
 523 the reductions caused become larger for smaller values of b_0/a_0 . This explains the
 524 specimen radius ratio (i.e. b_0/a_0) dependent behaviour that was observed in the cavity
 525 expansion curves of Fig. 3. Besides, the excess pore pressure generated at the inner cavity
 526 wall remains positive upon loading in normally consolidated soils, whereas it may
 527 become negative in heavily consolidated soils when the value of b_0/a_0 is sufficiently
 528 small. This is consistent with the experimental observations of Silvestri et al. [58] in
 529 laboratory pressuremeter tests with TWCs of undrained clay.

530 Fig. 6 also shows that, once the soil element enters the plastic state, the mean effective
 531 stress reduces gradually before resting on the CSL for soft clays (i.e. $R_0 < r^*$), and, in
 532 contrast, it increases with expansions for heavily overconsolidated clays (i.e. $R_0 > r^*$)
 533 until reaches the critical state value. Although the effective stress path varies with the soil
 534 model or the values of n and r^* used (e.g. Fig. 2) [22,40], it was found that the above
 535 conclusions about the effects of the b_0/a_0 value and the over-consolidation ratio to the
 536 cavity expansion response still validate for other models in Table 1. Therefore, results for
 537 other models are not presented here for brevity.

538 **4.2 Cavity closure under external loading**

539 In this subsection, the cavity closure response under external loading is discussed based
 540 on the results calculated using the solution for the CASM model (setting $n=2$ and $r^*=2$)
 541 with different values of the ratio of b_0/a_0 and the over-consolidation ratio. For illustration,
 542 stresses at both the inner and outer boundaries of a hollow cylinder or spherical shell are
 543 presented in Figs. 7-10, plotted against the volumetric strain of the inner cavity
 544 $(\Delta V / V_0)|_{r=a} = (a_0^{k+1} - a^{k+1}) / a_0^{k+1}$.

545 The soil mass moves inwards with increasing external pressure, while keeping the
 546 internal cavity pressure constant (Figs. 7-10). Initially, the total external pressure rises
 547 rapidly with cavity contractions; then the speed of the increase slows down, followed by
 548 a sharp increase when the inner cavity becomes very small or almost filled (for example,
 549 with $(\Delta V / V_0)|_{r=a}$ larger than 0.8 for a cylindrical cavity and 0.9 for a spherical cavity).

550 The external pressure required for compressing the soil to contract may decrease

551 significantly with a decreasing value of b_0/a_0 when it is smaller than a limit value, and
552 this disparity slightly varies with the deformation level. Similar to that observed in the
553 previous cavity expansion analysis, the limit ratio of b_0/a_0 , beyond which the boundary
554 effect to the cavity closure response become negligible, is also closely related to the stress
555 history and cavity shape in this loading program. The limit value of b_0/a_0 decreases with
556 increases of the over-consolidation ratio and is generally smaller for a spherical shell than
557 a hollow cylinder. For example, it is approximately 20 (Fig. 7) and 10 (Fig. 8) for a hollow
558 cylinder and spherical shell of normally consolidated soil (i.e. $R_0=1.001$), respectively,
559 and the corresponding values while $R_0=4$ are 10 (Fig. 9) and 5 (Fig. 10), respectively.

560 The effective stress state of soil is mainly dependent on the over-consolidation ratio
561 and local deformation. Once the soil element enters the plastic state, the mean effective
562 stress reduces gradually before resting on the CSL for soft clay, and, in contrast, it
563 increases gradually to the critical state value for heavily overconsolidated clay (Figs. 7-
564 10). With the same level of cavity contraction, the compatibility conditions of Eqs. (6)
565 and (11) describe that the shear strain at the outer boundary becomes smaller for a thicker
566 soil sample, which results in the observed difference in the effective stresses at $r=b$ in
567 Figs. 7-10. For example, the soil at $r=b$ may always remain elastic in a sufficiently thick
568 soil sample, whereas it yields plastically or enters the critical state easily while the
569 thickness of the surrounding soil is very thin.

570 As the soil goes through the same effective stress path and the internal cavity pressure
571 is kept constant in the external loading program, the stress path of soil particles at the
572 inner wall of the cavity for different values of b_0/a_0 overlap in Figs. 7-10 (i.e. blue lines).
573 Hence, at the same level of cavity contraction, the initial boundary values at $r=a$ for the
574 integration of the excess pore pressure remain unchanged for different values of b_0/a_0 .
575 However, the difference in the effective stresses between at $r=a$ and $r=b$ becomes
576 greater for a larger value of b_0/a_0 . As a result, greater excess pore pressure will be
577 generated at $r=b$ for a thicker soil cylinder or spherical shell according to Eq. (47),
578 which leads to the increase of the total external pressure with the value of b_0/a_0 in Figs. 7-
579 10. Although slight decreases may occur in a very thin cylinder or spherical shell of stiff
580 clays (e.g. Figs. 9d and 10d), during contractions the excess pore pressure at $r=b$
581 changes in a very similar way as the external cavity pressure.

582 **4.3 Cavity contraction under internal unloading**

583 For the prediction of soil behaviour around shallow tunnels, undrained solutions for a
584 cavity in a finite soil under the internal unloading program were derived by Zhuang et al.
585 [75], adopting the original and modified Cam-Clay models. To investigate the unloading
586 behaviour of TWCs, these solutions are also included in this paper together with the
587 solutions for the internal loading program and new solutions for the CASM model under
588 internal unloading. To briefly show the effect of the most relevant parameters (e.g. the
589 over-consolidation ratio and b_0/a_0 value) to unloading response, some results obtained
590 with the solution for the CASM model (taking $r^*=3$ and $n=2$) are presented in this
591 subsection. Detailed parametric studies into this problem with the Cam-Clay models refer
592 to Zhuang et al. [75].

593 Considering the surrounding soil as infinite (i.e. setting $a_0/b_0 \propto 0$), the present
594 unloading solution for the CASM model reduces to the solution of Mo and Yu [39].
595 Therefore, they produced identical results in this special case (Fig. 11). From the
596 comparison shown in Fig. 11, it can be concluded that: (a) The stability of the surrounding
597 soil (e.g. evaluated by $(p_0 - p_{in})/s_u$) [10] may drop significantly with smaller values of
598 b_0/a_0 , and a spherical shell of soil has higher stability than a hollow cylinder, keeping
599 other parameters the same. (b) A limit ratio of b_0/a_0 exists, beyond which the boundary
600 effect is negligible. The limit radius ratio for a spherical shell of soil is smaller than that
601 for a hollow cylinder, and it decreases slightly with the over-consolidation ratio. (c) The
602 degree of unloading in pressure (i.e. $(p_0 - p_{in})/p_0$) that the soil can sustain increases
603 with the over-consolidation ratio (i.e. the cavity stability can be improved as R_0 (or OCR)
604 increased). This is consistent with the experimental observations of wellbore instability
605 in undrained clays that were reported by Abdulhadi et al. [2].

606 **5 Prediction of soil behaviour in TWC tests**

607 To demonstrate the relevance of the derived solutions for modelling soil behaviour in
608 TWC tests, comparisons between predicted and measured results of cavity expansion and
609 contraction curves under each loading/unloading program are presented in this section.

610 **5.1 Prediction of pressuremeter curves in TWC tests**

611 Cavity expansion tests in a triaxial cylinder cell or calibration chamber have been widely
612 used to stimulate self-boring pressuremeter tests, and TWC apparatuses with a small
613 outer-to-inner diameter ratio (i.e. b_0/a_0) of 2 to 20 were often used in the laboratory

614 [1,6,26,33,34,58]. Fig. 3 showed that the undrained cavity expansion response may be
 615 greatly influenced by the outer constant-stress boundary while $b_0/a_0 < 20$. This has also
 616 been reported by Pyrah and Anderson [49] and Juran and Mahmoodzadegan [35], among
 617 others. In this subsection, a comparison between predicted and observed expansion curves
 618 for TWC tests reported by Frikha and Bouassida [26] is presented to validate the ability
 619 of the derived solutions on capturing the outer boundary effect (or b_0/a_0 effect) in the
 620 interpretation of laboratory pressuremeter tests.

621 A hollow cylinder cell of $D_i=20\text{mm}$, $D_o=100\text{mm}$ and $H/D_o=3$ was used in the
 622 undrained expansion tests of Frikha and Bouassida [26]. Keeping the outer confining
 623 pressure constant, the hollow cylinder specimens were loaded by increasing the internal
 624 cavity pressure. This conforms to the defined internal loading program. Therefore, the
 625 TWC test is simulated as an undrained cylindrical cavity expansion process based on the
 626 derived solutions for the internal loading analysis. The CASM model is used to describe
 627 the stress-strain behaviour of the normally consolidated Speswhite kaolin that used in the
 628 tests. With reference to the soil parameters that were reported by Atkinson et al. [7] and
 629 Frikha and Bouassida [26], model parameters of CASM are calibrated by simulating the
 630 undrained triaxial compression tests that were conducted with the same soil as shown in
 631 Fig. 12. It gives: $\Gamma = 3.14$, $\lambda = 0.136$, $\kappa = 0.025$, $\varphi_{tc} = 22.5^\circ$, $\mu = 0.3$, $n = 2$, and
 632 $r^* = 1.7 \square 2.0$.

633 To account for the shear mode effect, $\varphi_{cs} = 1.2\varphi_{tc}$ is taken in the cylindrical cavity
 634 expansion analysis [13]. For comparison, results without considering the shear mode
 635 effect (i.e. $\varphi_{cs} = \varphi_{tc}$) or the boundary effect (i.e. setting $b_0/a_0 \rightarrow \infty$, corresponding to the
 636 infinite solutions) were also calculated. Predicted and observed expansion curves are
 637 compared by plotting the net total cavity pressures ($p_{in} - p_0$) against the cavity
 638 volumetric strain $(\Delta V/V_0)|_{r=a}$ in Fig. 13. From Fig. 13, it can be concluded that the
 639 present finite solution can accurately predict the pressuremeter curves of undrained TWC
 640 tests with due consideration of the boundary effect and the shear mode effect. Without
 641 considering the finite thickness of the TWCs of soil, the infinite solution significantly
 642 over-predicts the cavity pressure, and the over-prediction becomes more serious at larger
 643 cavity expansions. On the contrary, the required expansion pressure is under-estimated
 644 when the shear mode effect is neglected.

645 By plotting pressuremeter results in terms of cavity pressure against the logarithm of
646 the volumetric strain, the plastic portion is almost a straight line (e.g. in the range of cavity
647 strains between 5 and 15%) for tests performed in large containers or ‘semi-infinite’ field
648 conditions, and the slope is often assumed to be equal to the undrained shear strength of
649 the soil [21,28,38]. However, Fig. 14 shows that this method is not always suitable for
650 the interpretation of laboratory pressuremeter tests in TWC apparatuses. An obvious
651 reduction in strength is observed due to the boundary effect while b_0/a_0 of the soil
652 specimen is smaller than 20. Yu [70] gave a comprehensive review of various sources of
653 inaccuracy that may exist in this simplified interpretation method, including effects of
654 pressuremeter geometry, water drainage conditions, strain rate and disturbance during
655 installation. The present study further demonstrates that attention should also be paid to
656 the outer boundary effect while small-sized hollow cylinder cells are used in laboratory
657 pressuremeter tests.

658 **5.2 Contraction response under internal unloading and external loading**

659 A series of TWC tests were performed by Abdulhadi [1] to investigate the wellbore
660 instability problem in soils under either internal unloading (e.g. TWC1 and TWC3) or
661 external loading (e.g. TWC2). Tests TWC1, TWC2 and TWC3 were chosen for the
662 comparison here as they were performed in fully saturated, uniform, isotropically
663 consolidated hollow cylinder specimens. The inner and outer diameters of the hollow
664 cylinder specimen were 25mm and 76mm, respectively. The specimen height was
665 152mm, and it has been verified that this height to outer diameter ratio ($H/D_0=2$)
666 produced a minimal impact on the borehole response [3], which fulfils the plane strain
667 assumption. Reconstituted Boston blue clay (RBBC) was used in the tests. To determine
668 the soil parameters in CASM, the triaxial compression test on isotropically consolidated
669 RBBC that reported by Ladd [37] is simulated as shown in Fig. 15. It gives: $\Gamma = 2.671$,
670 $\lambda = 0.184$, $\kappa = 0.01$, $\mu = 0.28$, $\varphi_{tc} = 33.4^\circ$, $n = 1.5$, and $r^* = 2.1$. The soil parameters
671 were determined by cross-referencing to the oedometric test data reported by Abdulhadi
672 [1] and those summarised by Akl and Whittle [4]. These tests are simulated as a
673 cylindrical cavity contraction process using the derived solutions. The same set of model
674 parameters were used in the model predictions, and $R_0=1.001$ was taken as the soil
675 specimens were normally consolidated.

676 Predicted and measured cavity contraction curves for tests performed under internal
677 unloading and external loading are compared in Figs. 16 and 17, respectively. In tests
678 TWC1 and TWC3, the soil cylinder contracts due to the internal unloading (Fig. 16).
679 Instead, the specimen deforms inwards driven by the external compression in test TWC2
680 (Fig. 17). Compared to the experimental data, the theoretical solutions tend to
681 underestimate soil stiffness during the initial contractions in both cases. A comparison
682 between the idealised cavity contraction models and the experimental observations
683 indicates that this discrepancy may be attributed to the following aspects. Firstly, it was
684 observed that the pore pressures were not fully equilibrated across the width of the clay
685 specimen with a loading or unloading rate of 10%/hour (approximately 80-90%
686 equilibrated [2]). In other words, the applied pressures at the boundaries cannot transfer
687 through the whole soil specimen immediately. Secondly, the predicted effective stress
688 paths within soil slightly deviate from that occurred in the tests. Although RBBC has been
689 used at MIT (Massachusetts Institute of Technology) for over 50 years, the raw Boston
690 clay, the re-sedimentation procedure and consolidation pressures during sample
691 preparations in the triaxial compression tests of Ladd [37] and the TWC tests of
692 Abdulhadi [1] were not exactly the same, which may lead to some deviations in the stress-
693 strain behaviour. Moreover, the inherent boundary effect caused during sample
694 preparation and the rate dependence in soil behaviour, which are ignored in the present
695 model, may also result in differences between physical tests and theoretical models more
696 or less [2]. It seems that the overall influences of the above factors produced relatively
697 greater influences on the initial contraction response as the predicted and measured results
698 are in close agreement at relatively large deformations (e.g. the steady contraction stage).
699 Nevertheless, the comparisons in Figs. 16 and 17 indicate that, with due consideration of
700 the shear mode effect, the predicted cavity contraction curves under either internal
701 unloading or external loading are basically consistent with those measured in the tests, in
702 particular, at the steady contraction stage (or the most vulnerable stage) which is of great
703 concern for the borehole instability analysis. If the boundary effect is ignored (e.g. in the
704 infinite solution), the soil stability under internal unloading could be significantly over-
705 predicted (Fig. 16).

706 Tests TWC1 and TWC3 were performed with the same initial confining pressures. It
707 is interesting to note these two tests show similar soil stability results if evaluated in terms
708 of $(p_{\text{out}} - p_{\text{in}}) / s_u$. However, the total stress paths or excess pore pressures are essentially

709 different in these two cases as also highlighted by Abdulhadi [1]. In addition, the results
710 in Figs. 16 and 17 indicate that the back-calculated critical state friction angle φ_{cs} from
711 the test under internal unloading (e.g. TWC1) is slightly smaller than that based on the
712 test under external loading (e.g. TWC1). This minor difference might be caused by the
713 loading path effect, but this needs to be justified with more experimental evidence.

714 It should be pointed out that, in previous TWC tests, the pore pressure is mostly
715 measured at the axial ends and only assumed average values across the width of the
716 specimen are available. Therefore, only the total stresses are compared in the above cases.
717 As a consequence, possible influences of local consolidation and rate-dependent
718 redistribution of the pore pressure cannot be evaluated from these experimental results.
719 These effects might be significant, in particular, for tests with relatively thick soil
720 samples, and direct detection of them could be very useful for the investigation on
721 relevant soil properties (e.g. hydraulic properties). Therefore, it is believed that TWC test
722 apparatus equipped with more advanced imaging techniques such as X-ray Computed
723 Tomography [36,41,59] can offer additional insight into the soil behaviour involved due
724 to its ability to probe the 3D in situ soil porous architecture at high resolutions (i.e. 1 μm).

725 **6 | Conclusions**

726 We have presented a general solution procedure for undrained loading and unloading
727 analyses of both cylindrical and spherical cavities embedded in soils with a finite radial
728 extent, which is applicable to many two-invariant critical state soil models. Three stress-
729 controlled loading programs (internal loading, internal unloading and external loading)
730 that are commonly used in TWC tests are considered. Following the proposed procedure,
731 a set of large strain analytical/semi-analytical cavity expansion and contraction solutions
732 are derived for several critical state soil models, which can provide valuable benchmark
733 for verifying various numerical programs. The derived solutions are used to investigate
734 the boundary effect (or specimen size effect) to the cavity expansion and contraction
735 responses. It is shown that a limit value of b_0/a_0 exists in each loading/unloading program,
736 below which the boundary effect could lead to significant reductions in the degree of
737 loading or unloading that the surrounding soil can sustain. Although the limit value of
738 b_0/a_0 may vary with the over-consolidation ratio and the cavity deformation level, it was
739 found that, in general, $b_0/a_0 \geq 20$ is a minimum practical requirement to remove the

740 boundary effect in common TWC tests under undrained conditions, and this value is much
741 smaller for a spherical shell of soil (approximately $b_0 / a_0 \geq 10$).

742 Using the published results of several TWC tests under different stress-controlled
743 loading/unloading programs in the literature, comparisons between predicted and
744 measured cavity expansion and contraction curves are made. Overall, the theoretical
745 predictions show satisfactory agreement with the experimental data. The results of these
746 comparisons suggest that the proposed cylindrical solutions are able to capture the
747 boundary effect that is commonly observed in undrained TWC tests under the considered
748 three loading/unloading programs. This is essential for the interpretation of laboratory
749 TWC tests. Inversely, the finite cavity expansion and contraction solutions may be
750 calibrated or validated with relevant TWC tests which require less energy, time and space
751 than site tests. Then setting $b_0 / a_0 \propto \infty$, the calibrated solutions can be used to simulate
752 field pressuremeter tests and investigate the in-situ wellbore instability problem as the
753 infinite cavity expansion or contraction solutions often did [14,18,71].

754 **Acknowledgements**

755 The authors would like to acknowledge the Open Research Fund of the State Key
756 Laboratory for Geomechanics and Deep Underground Engineering China University of
757 Mining and Technology (SKLGDUEK1802) and the International Mobility Fund from
758 the University of Leeds. The first author also acknowledges the support of the ‘Taishan’
759 Scholar Program of Shandong Province, China (No. tsqn201909016) and the ‘Qilu’
760 Scholar Program of Shandong University.

761 **References**

- 762 1. Abdulhadi NO (2009) An experimental investigation into the stress-dependent
763 mechanical behavior of cohesive soil with application to wellbore instability. PhD
764 thesis, Massachusetts Institute of Technology, Cambridge, MA, USA
- 765 2. Abdulhadi NO, Germaine JT, Whittle AJ (2010) Experimental study of wellbore
766 instability in clays. *Journal of Geotechnical and Geoenvironmental Engineering* 137
767 (8):766-776
- 768 3. Abdulhadi NO, Germaine JT, Whittle AJ (2011) Thick-walled cylinder testing of clays
769 for the study of wellbore instability. *Geotechnical Testing Journal* 34 (6):746-754
- 770 4. Akl SA, Whittle AJ (2016) Validation of soil models for wellbore stability in ductile
771 formations using laboratory TWC tests. *Journal of Geotechnical and*
772 *Geoenvironmental Engineering* 143 (2):04016095
- 773 5. Alsiny A, Vardoulakis I, Drescher A (1992) Deformation localization in cavity
774 inflation experiments on dry sand. *Geotechnique* 42 (3):395-410
- 775 6. Anderson WF, Pyrah IC, Ali FH (1987) Rate effects in pressuremeter tests in clays.
776 *Journal of Geotechnical Engineering* 113 (11):1344-1358
- 777 7. Atkinson J, Richardson D, Robinson P (1987) Compression and extension of K 0
778 normally consolidated kaolin clay. *Journal of Geotechnical Engineering* 113
779 (12):1468-1482
- 780 8. Au AS, Yeung AT, Soga K (2006) Pressure-controlled cavity expansion in clay.
781 *Canadian Geotechnical Journal* 43 (7):714-725
- 782 9. Augarde CE, Lyamin AV, Sloan SW (2003) Prediction of undrained sinkhole collapse.
783 *Journal of Geotechnical and Geoenvironmental Engineering* 129 (3):197-205
- 784 10. Broms BB, Bennermark H (1967) Stability of clay at vertical openings. *Journal of*
785 *Soil Mechanics & Foundations Division* 93 (1):71-94
- 786 11. Carter JP (1978) CAMFE, a computer program for the analysis of a cylindrical cavity
787 expansion in soil. Report CUED/C–Soils TR52, Department of Engineering,
788 University of Cambridge, Cambridge, UK
- 789 12. Carter JP, Booker JR, Yeung SK (1986) Cavity expansion in cohesive frictional soils.
790 *Geotechnique* 36 (3):349-358
- 791 13. Chang M-F, Teh CI, Cao L (1999) Critical state strength parameters of saturated clays
792 from the modified Cam clay model. *Canadian Geotechnical Journal* 36 (5):876-890

- 793 14. Charlez PA, Roatesi S (1999) A fully analytical solution of the wellbore stability
794 problem under undrained conditions using a linearised Cam-Clay model. *Oil & Gas*
795 *Science and Technology* 54 (5):551-563
- 796 15. Chen SL, Abousleiman YN (2012) Exact undrained elasto-plastic solution for
797 cylindrical cavity expansion in modified Cam Clay soil. *Geotechnique* 62 (5):447-
798 456
- 799 16. Chen SL, Abousleiman YN (2013) Exact drained solution for cylindrical cavity
800 expansion in modified Cam Clay soil. *Geotechnique* 63 (6):510-517
- 801 17. Chen SL, Abousleiman YN (2016) Drained and undrained analyses of cylindrical
802 cavity contractions by bounding surface plasticity. *Canadian Geotechnical Journal* 53
803 (9):1398-1411
- 804 18. Chen SL, Abousleiman YN (2017) Wellbore stability analysis using strain hardening
805 and/or softening plasticity models. *International Journal of Rock Mechanics and*
806 *Mining Sciences* 93:260-268
- 807 19. Cheng Y, Yang H-W (2019) Exact solution for drained spherical cavity expansion in
808 saturated soils of finite radial extent. *International Journal for Numerical and*
809 *Analytical Methods in Geomechanics* 43:1594–1611. doi:doi: org/10.1002/nag.2924
- 810 20. Cheng Y, Yang H-W, Sun DA (2018) Cavity expansion in unsaturated soils of finite
811 radial extent. *Computers and Geotechnics* 102:216-228
- 812 21. Clarke BG (1993) The interpretation of self-boring pressuremeter tests to produce
813 design parameters. Paper presented at the Predictive soil mechanics: Proceedings of
814 the Wroth Memorial Symposium, London, UK,
- 815 22. Collins IF, Yu HS (1996) Undrained cavity expansions in critical state soils.
816 *International Journal for Numerical and Analytical Methods in Geomechanics* 20
817 (7):489-516
- 818 23. Doreau-Malioche J, Combe G, Viggiani G, Toni J (2018) Shaft friction changes for
819 cyclically loaded displacement piles: an X-ray investigation. *Géotechnique Letters* 8
820 (1):66-72
- 821 24. Durban D, Papanastasiou P (1997) Cylindrical cavity expansion and contraction in
822 pressure sensitive geomaterials. *Acta mechanica* 122:99-122
- 823 25. Fahey M (1986) Expansion of a thick cylinder of sand: a laboratory simulation of the
824 pressuremeter test. *Geotechnique* 36 (3):397-424

- 825 26. Frikha W, Bouassida M (2015) Comparison between results of triaxial shear test and
826 expansion of cavity in hollow cylinder. Paper presented at the ISP7-Pressio 2015,
827 Hammaet, Tunisia,
- 828 27. Ghionna VN, Jamiolkowski M A critical appraisal of calibration chamber testing of
829 sands. In: the First International Symposium on Calibration Chamber Testing,
830 Potsdam, New York, 1991. Elsevier, pp 13-40
- 831 28. Gibson RE, Anderson WF (1961) In situ measurement of soil properties with the
832 pressuremeter. *Civil Engineering and Public Works Review* 56 (658):615-618
- 833 29. Goodarzi M, Stähler F, Kreiter S, Rouainia M, Kluger M, Mörz T (2018) Numerical
834 simulation of cone penetration test in a small-volume calibration chamber: The effect
835 of boundary conditions. Paper presented at the 4th International Symposium on Cone
836 Penetration Testing (CPT 2018), Delft, the Netherlands,
- 837 30. Hill R (1950) *The mathematical theory of plasticity*. Oxford University Press, London
- 838 31. Huang AB, Holtz RD, Chameau JL (1991) Laboratory study of pressuremeter tests in
839 clays. *Journal of Geotechnical Engineering* 117 (10):1549-1567
- 840 32. Hughes JMO, Wroth CP, Windle D (1977) Pressuremeter tests in sands. *Geotechnique*
841 27 (4):455-477
- 842 33. Jewell R, Fahey M, Wroth C (1980) Laboratory studies of the pressuremeter test in
843 sand. *Geotechnique* 30 (4):507-531
- 844 34. Juran I, BenSaid M (1987) Cavity expansion tests in a hollow cylinder cell.
845 *Geotechnical Testing Journal* 10 (4):203-212
- 846 35. Juran I, Mahmoodzadegan B (1990) Laboratory measurement of lateral stress induced
847 by a cavity expansion in a hollow cylinder cell. *Transportation Research Record*
848 (1278):204-214
- 849 36. Labiouse V, Sauthier C, You S (2014) Hollow cylinder simulation experiments of
850 galleries in boom clay formation. *Rock Mechanics and Rock Engineering* 47 (1):43-
851 55
- 852 37. Ladd C (1965) Stress-strain behaviour of anisotropically consolidated clays during
853 undrained shear. Paper presented at the Proceedings of the 6th International
854 Conference on Soil Mechanics and Foundation Engineering, Montréal,
- 855 38. Mair RJ, Wood DM (1987) *Pressuremeter testing: methods and interpretation*. CIRIA-
856 Butterworths, London, UK

- 857 39. Mo PQ, Yu HS (2017) Undrained Cavity-Contraction Analysis for Prediction of Soil
858 Behavior around Tunnels. *International Journal of Geomechanics* 17 (5):04016121-
859 04016121-04016110. doi:DOI: 10.1061/(ASCE)GM.1943-5622.0000816.
- 860 40. Mo PQ, Yu HS (2017) Undrained cavity expansion analysis with a unified state
861 parameter model for clay and sand. *Geotechnique* 67 (6):503-515. doi:DOI:
862 10.1680/jgeot.15.P.261.
- 863 41. Mooney SJ (2002) Three - dimensional visualization and quantification of soil
864 macroporosity and water flow patterns using computed tomography. *Soil Use and*
865 *Management* 18 (2):142-151
- 866 42. Palmer AC (1971) Undrained plane-strain expansion of a cylindrical cavity in clay: a
867 simple interpretation of the pressuremeter test. Division of Engineering, Brown
868 University, Providence, RI, USA
- 869 43. Paniagua P, Andò E, Silva M, Emdal A, Nordal S, Viggiani G (2013) Soil deformation
870 around a penetrating cone in silt. *Géotechnique Letters* 3 (4):185-191
- 871 44. Papamichos E (2010) Borehole failure analysis in a sandstone under anisotropic
872 stresses. *International Journal for Numerical and Analytical Methods in*
873 *Geomechanics* 34 (6):581-603
- 874 45. Papamichos E, Tronvoll J, Skjærstein A, Unander TE (2010) Hole stability of Red
875 Wildmoor sandstone under anisotropic stresses and sand production criterion. *Journal*
876 *of Petroleum Science and Engineering* 72 (1-2):78-92
- 877 46. Perić D, Ayari MA (2002) On the analytical solutions for the three-invariant Cam
878 clay model. *International Journal of Plasticity* 18 (8):1061-1082
- 879 47. Pournaghiazar M, Russell AR, Khalili N (2012) Linking cone penetration resistances
880 measured in calibration chambers and the field. *Géotechnique Letters* 2 (2):29-35
- 881 48. Pournaghiazar M, Russell AR, Khalili N (2013) Drained cavity expansions in soils of
882 finite radial extent subjected to two boundary conditions. *International Journal for*
883 *Numerical and Analytical Methods in Geomechanics* 37 (4):331-352
- 884 49. Pyrah IC, Anderson WF (1990) Numerical assessment of self-boring pressuremeter
885 tests in a clay calibration chamber. Paper presented at the Proceedings of the Third
886 International Symposium on Pressuremeters, London, UK,
- 887 50. Roscoe KH, Burland JB (1968) On the generalized stress-strain behaviour of wet clay.
888 In: Heymann G, Leckie FA (eds) *Engineering Plasticity*. Cambridge University Press,
889 London, UK, pp 535-609

- 890 51. Roscoe KH, Schofield AN (1963) Mechanical behaviour of an idealized 'wet' clay.
891 Paper presented at the Proceedings of the 3rd European Conference on Soil
892 Mechanics and Foundation Engineering,
- 893 52. Roscoe KH, Schofield AN, Wroth CP (1958) On the yielding of soils. *Geotechnique*
894 8 (1):22-53
- 895 53. Salgado R, Mitchell JK, Jamiolkowski M (1997) Cavity expansion and penetration
896 resistance in sand. *Journal of Geotechnical and Geoenvironmental Engineering* 123
897 (4):344-354
- 898 54. Salgado R, Mitchell JK, Jamiolkowski M (1998) Calibration chamber size effects on
899 penetration resistance in sand. *Journal of Geotechnical and Geoenvironmental*
900 *Engineering* 124 (9):878-888
- 901 55. Schnaid F, Houlsby G (1991) An assessment of chamber size effects in the calibration
902 of in situ tests in sand. *Geotechnique* 41 (3):437-445
- 903 56. Sheng D, Sloan SW, Yu HS (2000) Aspects of finite element implementation of
904 critical state models. *Computational Mechanics* 26 (2):185-196
- 905 57. Silvestri V (1998) On the determination of the stress-strain curve of clay from the
906 undrained plane-strain expansion of hollow cylinders: a long-forgotten method.
907 *Canadian Geotechnical Journal* 35 (2):360-363
- 908 58. Silvestri V, Diab R, Ducharme A (2005) Development of a new hollow cylinder
909 triaxial apparatus for the study of expansion tests in clay. *Geotechnical Testing*
910 *Journal* 28 (3):231-239
- 911 59. Tracy SR, Daly KR, Sturrock CJ, Crout NM, Mooney SJ, Roose T (2015) Three -
912 dimensional quantification of soil hydraulic properties using X - ray Computed
913 Tomography and image - based modeling. *Water Resources Research* 51 (2):1006-
914 1022
- 915 60. van Nes JHG (2004) Application of computerized tomography to investigate strain
916 fields caused by cone penetration in sand. Master Dissertation, Delft University of
917 Technology, Delft, the Netherlands
- 918 61. Vrakas A (2016) A rigorous semi - analytical solution for undrained cylindrical
919 cavity expansion in critical state soils. *International Journal for Numerical and*
920 *Analytical Methods in Geomechanics* 40 (15):2137-2160

- 921 62. Vrakas A, Anagnostou G (2015) Finite strain elastoplastic solutions for the undrained
922 ground response curve in tunnelling. *International Journal for Numerical and*
923 *Analytical Methods in Geomechanics* 39 (7):738-761
- 924 63. Wang CL, Zhou H, Liu HL, Ding XM (2019) Analysis of undrained spherical cavity
925 expansion in modified Cam Clay of finite radial extent. *European Journal of*
926 *Environmental and Civil Engineering*:1-12.
927 doi:org/10.1080/19648189.2019.1687015
- 928 64. Wood DM (1990) *Soil behaviour and critical state soil mechanics*. Cambridge
929 University Press, Cambridge, UK
- 930 65. Wroth CP (1984) The interpretation of in situ soil tests. *Geotechnique* 34 (4):449-489
- 931 66. Yu HS (1992) Expansion of a thick cylinder of soils. *Computers and Geotechnics* 14
932 (1):21-41
- 933 67. Yu HS (1993) Finite elastoplastic deformation of an internally pressurized hollow
934 sphere. *Acta Mechanica Solida Sinica (English Edition)* 6 (1):81-97
- 935 68. Yu HS (1998) CASM: A unified state parameter model for clay and sand.
936 *International Journal for Numerical and Analytical Methods in Geomechanics* 22
937 (8):621-653
- 938 69. Yu HS (2000) *Cavity expansion methods in geomechanics*. Kluwer Academic
939 Publishers, Dordrecht, the Netherlands
- 940 70. Yu HS (2006) The First James K. Mitchell Lecture: In situ soil testing: from
941 mechanics to interpretation. *Geomechanics and Geoengineering: An International*
942 *Journal* 1 (3):165-195
- 943 71. Yu HS, Collins IF (1998) Analysis of self-boring pressuremeter tests in
944 overconsolidated clays. *Geotechnique* 48 (5):689-693
- 945 72. Yu HS, Houlsby GT (1991) Finite cavity expansion in dilatant soils: loading analysis.
946 *Geotechnique* 41 (2):173-183
- 947 73. Yu HS, Rowe RK (1999) Plasticity solutions for soil behaviour around contracting
948 cavities and tunnels. *International Journal for Numerical and Analytical Methods in*
949 *Geomechanics* 23 (12):1245-1279
- 950 74. Zervos A, Papanastasiou P, Vardoulakis I (2001) Modelling of localisation and scale
951 effect in thick-walled cylinders with gradient elastoplasticity. *International Journal of*
952 *Solids and Structures* 38 (30):5081-5095

953 75. Zhuang PZ, Yang H, Yu HS, Fuentes R, Song XG (2019) Plasticity solutions for
954 predictions of undrained stability and ground deformation of shallow tunnels in clay.
955 Tunnelling and Underground Space Technology:(under review)

956 **Figure captions**

957 Fig.1. Schematic of a thick-walled cylinder.

958 Fig.2. Example yield surfaces of Cam-Clay models and CASM.

959 Fig.3. Total pressure and excess pore pressure at the inner cavity of modified Cam clay:
960 (a) cylindrical solution with $R_0=1.001$; (b) spherical solution with $R_0=1.001$; (c)
961 cylindrical solution with $R_0=4$; (d) spherical solution with $R_0=4$; (e) cylindrical solution
962 with $R_0=16$; (f) spherical solution with $R_0=16$.

963 Fig.4. Stress distribution in modified Cam clay with $R_0=1.001$: (a) cylindrical model in
964 an infinite soil mass; (b) spherical model in an infinite soil mass; (c) cylindrical model
965 with small values of b_0/a_0 ; (d) spherical model with small values of b_0/a_0 .

966 Fig.5. Stress distribution in modified Cam clay with $R_0=16$: (a) cylindrical model in an
967 infinite soil mass; (b) spherical model in an infinite soil mass; (c) cylindrical model with
968 small values of b_0/a_0 ; (d) spherical model with small values of b_0/a_0 .

969 Fig.6. Typical stress paths in modified Cam clay: (a) cylindrical model with $b_0/a_0=1000$;
970 (b) spherical model with $b_0/a_0=1000$; (c) cylindrical model with $b_0/a_0=2$; (d) spherical
971 model with $b_0/a_0=2$.

972 Fig.7. A thick-walled cylinder of normally consolidated London clay ($R_0=1.001$) under
973 external loading.

974 Fig.8. A spherical shell of normally consolidated London clay ($R_0=1.001$) under
975 external loading.

976 Fig.9. A thick-walled cylinder cavity of stiff London clay ($R_0=4$) under external loading.

977 Fig.10. A spherical shell of stiff London clay ($R_0=4$) under external loading.

978 Fig.11. Cavity contraction curves under internal unloading: (a) and (c) cylindrical
979 model; (b) and (d) spherical model.

980 Fig.12. Model prediction for undrained triaxial compression tests with soft Speswhite
981 kaolin.

982 Fig.13. Predicted and measured cavity expansion curves in a thick-walled cylinder of
983 kaolin clay.

984 Fig.14. Pressuremeter curves with different values of b_0/a_0 (Speswhite kaolin).

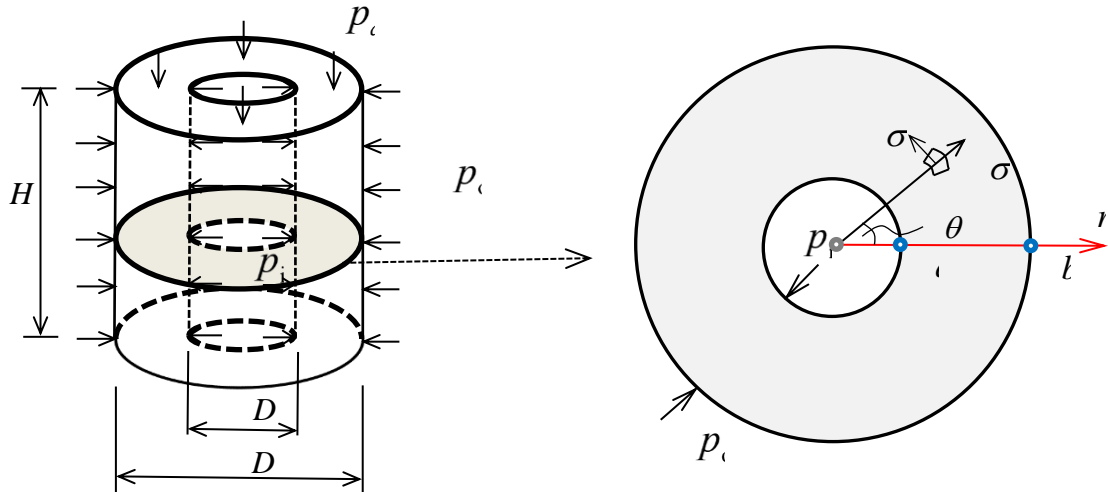
985 Fig.15. Model prediction for an undrained triaxial compression test on isotropically
986 consolidated RBBC.

987 Fig.16. Predicted and measured cavity contraction curves in thick-walled cylinders of
988 RBBC under internal unloading.

989 Fig.17. Predicted and measured cavity contraction curves in a thick-walled cylinder of
990 RBBC under external loading.

| | | |
|------|---|---|
| 991 | Notation | |
| 992 | p_a, p_{in}, p_{out} | axial stress, internal and external radial pressures |
| 993 | ζ | $\zeta = 1$ for loading and $\zeta = -1$ for unloading |
| 994 | k | $k = 1$ for a cylindrical cavity and $k = 2$ for a spherical cavity |
| 995 | r, θ, z | coordinates of the cylindrical coordinate system |
| 996 | r, θ, φ | coordinates of the spherical coordinate system |
| 997 | r_0 | initial value of the radial co-ordinate r |
| 998 | p', q | mean effective stress and deviatoric stress |
| 999 | p'_{cs}, q_{cs} | mean effective stress and deviatoric stress at the critical state |
| 1000 | p | mean total pressure |
| 1001 | p_0, p'_0 | initial values of p and p' |
| 1002 | $U, U_0, \Delta U$ | total, initial ambient, excess pore pressures |
| 1003 | $\Delta U _{r=a}, \Delta U _{r=b}$ | excess pore pressures at $r = a$ and at $r = b$ |
| 1004 | $\Delta U _{r=c}, \Delta U _{r=r_{cs}}$ | excess pore pressures at $r = c$ and at $r = r_{cs}$ |
| 1005 | $\sigma'_r, \sigma'_\theta$ | effective radial and circumferential stresses |
| 1006 | σ_r, σ_θ | total radial and circumferential stresses |
| 1007 | $\varepsilon_r, \varepsilon_\theta$ | radial and circumferential strains |
| 1008 | δ, γ | volumetric and shear strains |
| 1009 | $a_0, a; b_0, b; c_0, c$ | initial and current radii of the inner cavity wall, the outer cavity |
| 1010 | | wall, the elastic-plastic boundary |
| 1011 | r_{cs} | radius of the plastic-critical state boundary |
| 1012 | p'_a, q_a | mean effective and shear stresses at $r = a$ |
| 1013 | p'_b, q_b | mean effective and shear stresses at $r = b$ |
| 1014 | γ_a, γ_b | shear strains at $r = a$ and at $r = b$ |
| 1015 | γ_{ep}, q_{ep} | shear strain and shear stress at the state just enters plastic yielding |
| 1016 | K, G | instantaneous bulk and shear moduli with initial values of K_0 and |
| 1017 | | G_0 |
| 1018 | M | the slope of the CSL in the $p' - q$ space |
| 1019 | λ | slope of the normally compression line |
| 1020 | Γ | the value of v on the CSL at $p' = 1\text{kPa}$ |

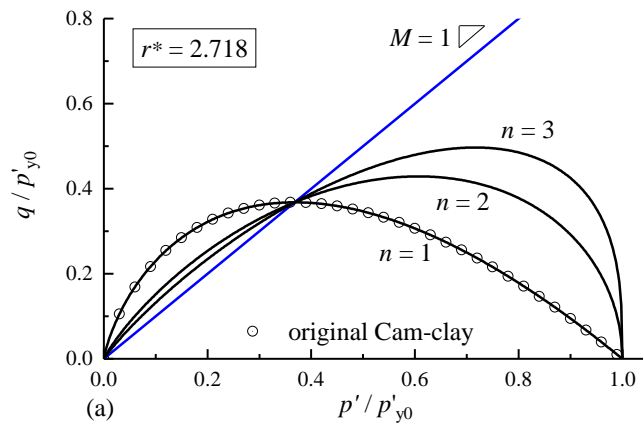
| | | |
|------|-------------------|--|
| 1021 | v, μ | specific volume and Poisson's ratio of soil |
| 1022 | κ | slope of the swelling line |
| 1023 | Λ | plastic volumetric strain ratio, equals $(\lambda - \kappa)/\lambda$ |
| 1024 | R_0 | isotropic over-consolidation ratio, defines as p'_{y0} / p'_0 |
| 1025 | n, r^* | stress-state coefficient and spacing ratio in CASM |
| 1026 | p'_y, p'_{y0} | preconsolidation pressure and its initial value |
| 1027 | s_u | undrained shear strength of soil |
| 1028 | η, η_{ep} | stress ratio and its value at the elastic-plastic boundary |
| 1029 | ϕ_{cs} | critical state friction angle, Hvorslev friction angle |
| 1030 | ϕ_{tc} | critical state friction angle under triaxial compression and plane |
| 1031 | | strain |
| 1032 | $\Delta V / V_0$ | cavity volumetric strain |
| 1033 | | |



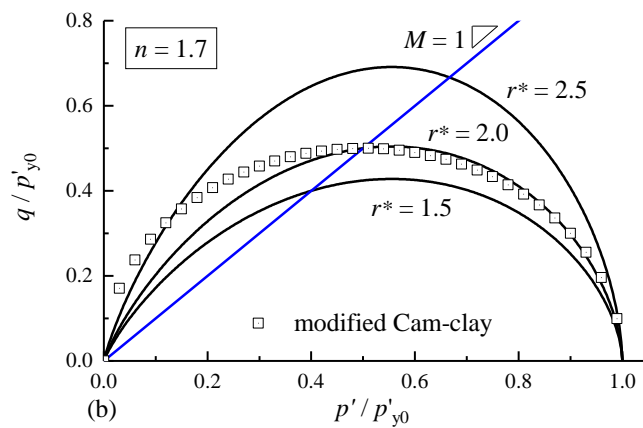
1034

1035 Fig 1 Schematic of a thick-walled cylinder

1036



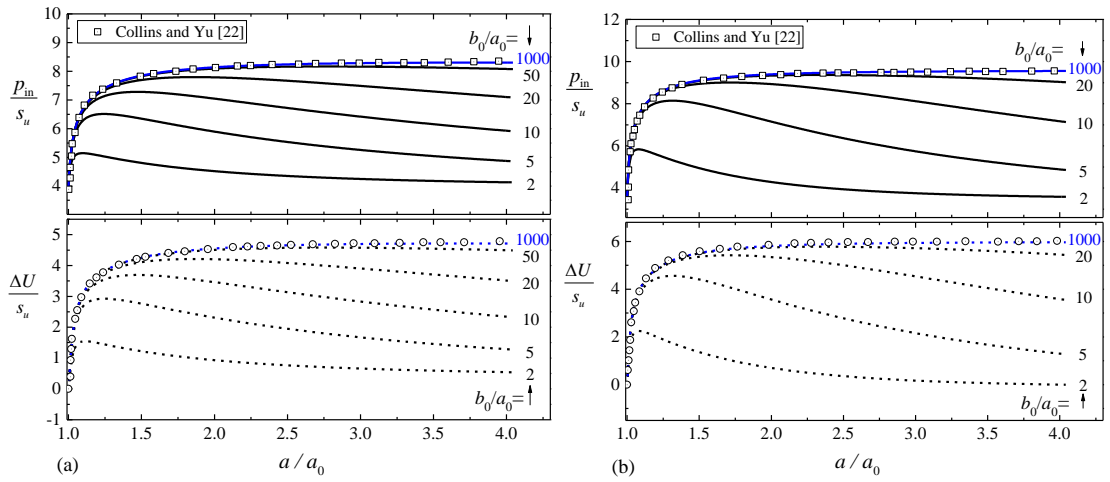
1037



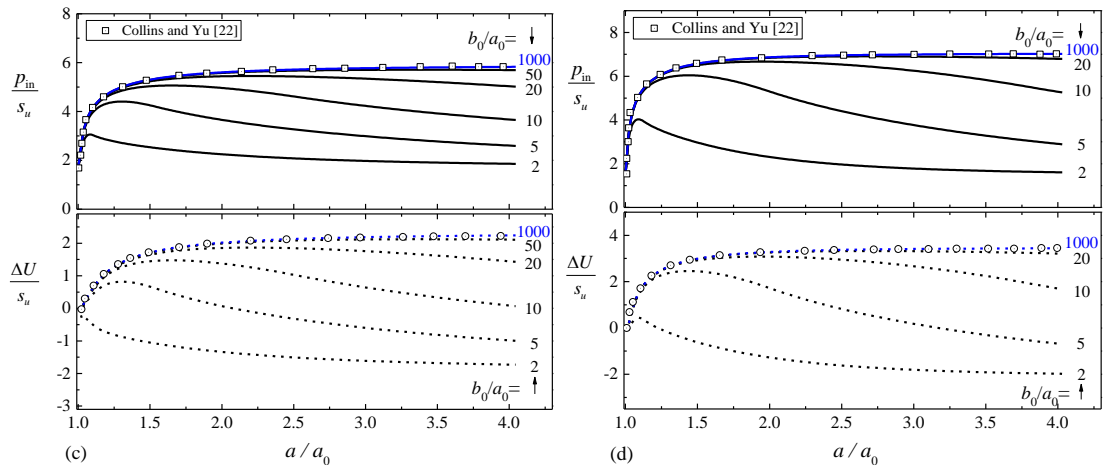
1038

1039 Fig 2 Example yield surfaces of Cam-clay models and CASM.

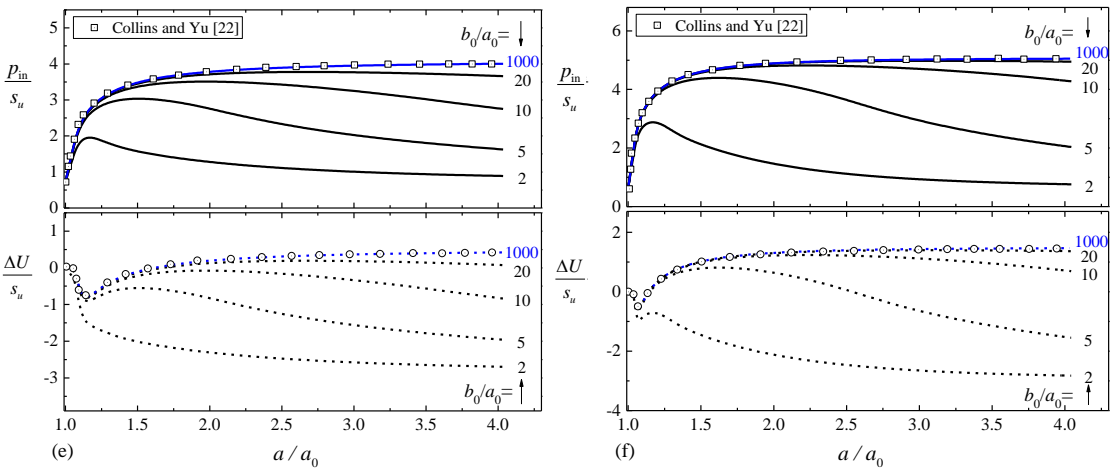
1040



1041



1042

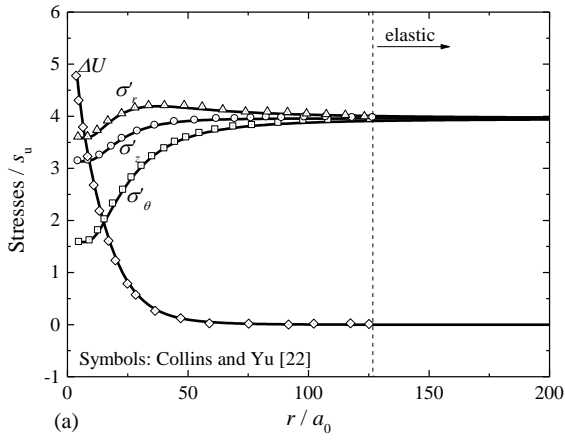


1043 Fig. 3. Total pressure and excess pore pressure at the inner cavity of modified Cam clay:
 1044 (a) cylindrical solution with $R_0=1.001$; (b) spherical solution with $R_0=1.001$; (c)
 1045 cylindrical solution with $R_0=4$; (d) spherical solution with $R_0=4$; (e) cylindrical solution
 1046 with $R_0=16$; (f) spherical solution with $R_0=16$.

1047

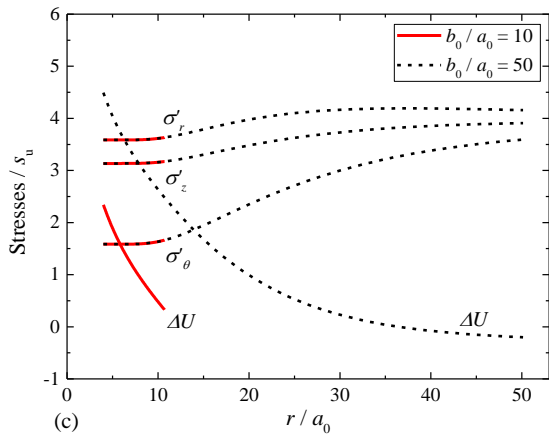
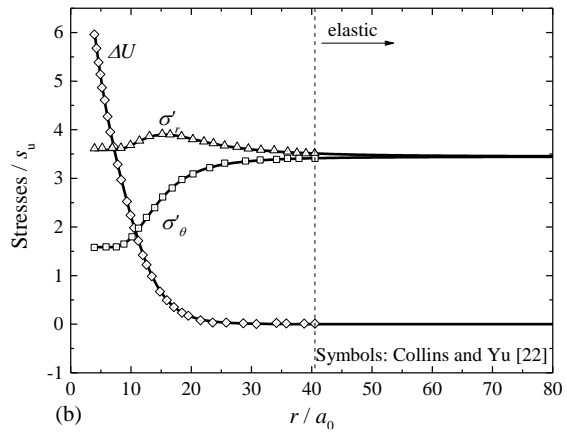
1048

1049

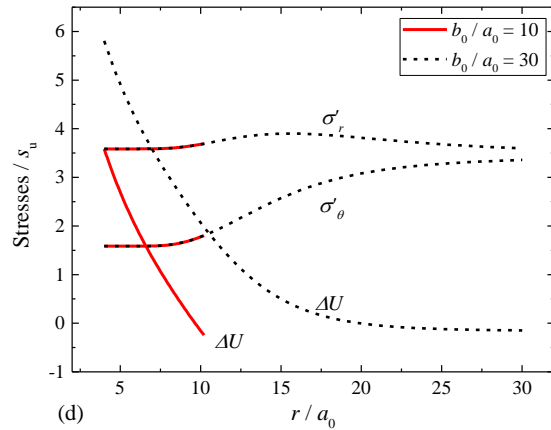


1050

1051

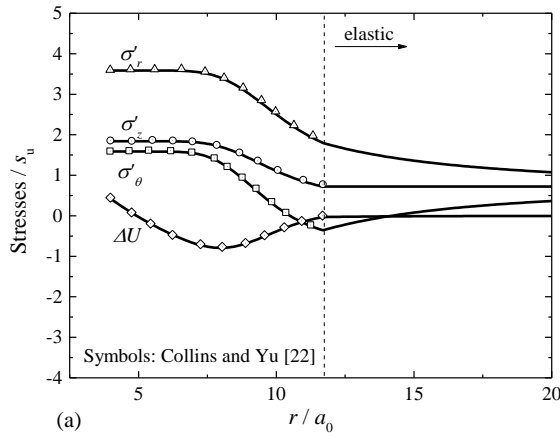


1052

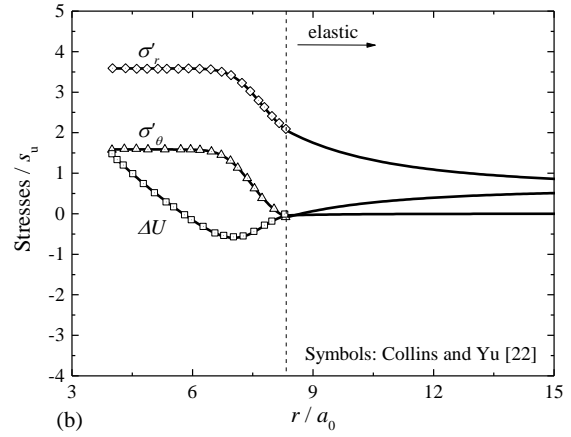


1053 Fig. 4. Stress distribution in modified Cam clay with $R_0=1.001$: (a) cylindrical model in
1054 an infinite soil mass; (b) spherical model in an infinite soil mass; (c) cylindrical model
1055 with small values of b_0/a_0 ; (d) spherical model with small values of b_0/a_0 .

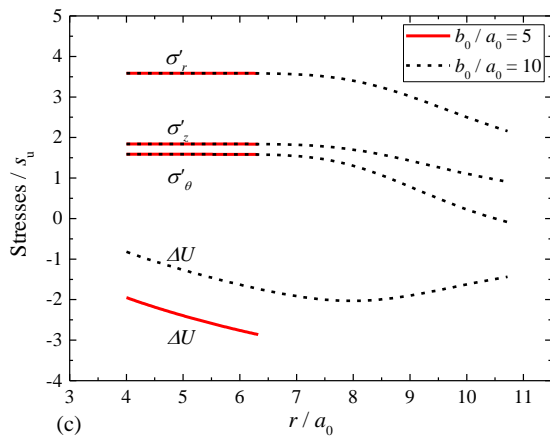
1056



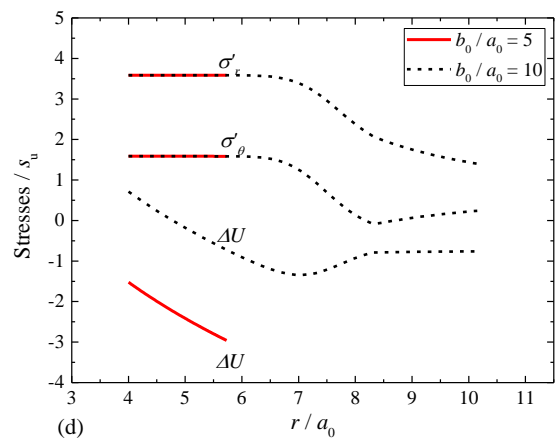
1057



1058

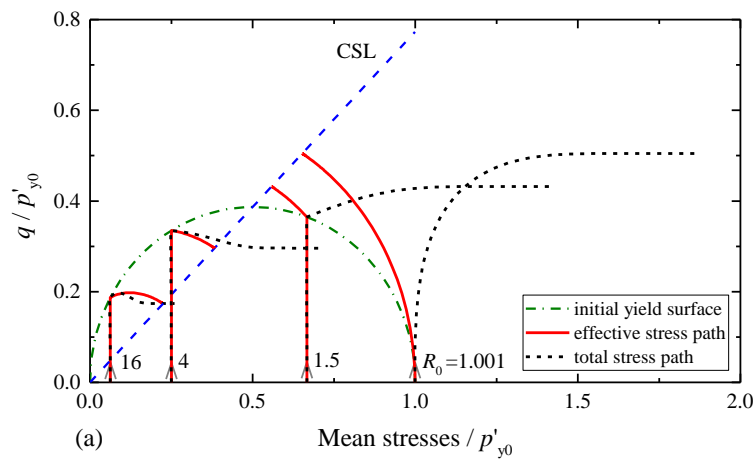


1059

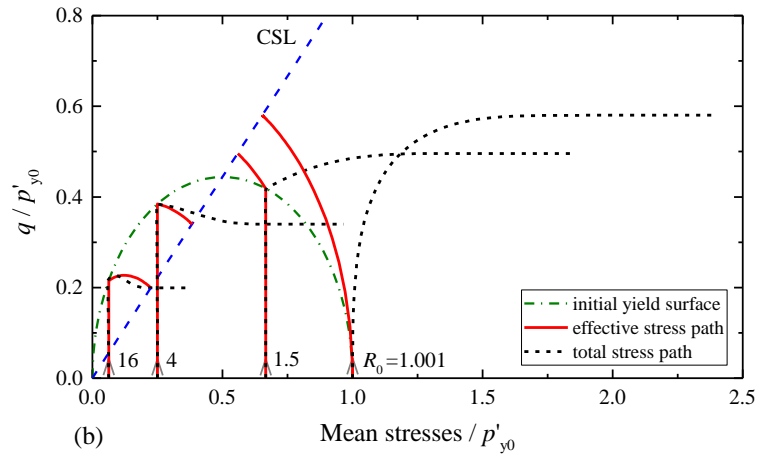


1060 Fig. 5. Stress distribution in modified Cam clay with $R_0=16$: (a) cylindrical model in an
 1061 infinite soil mass; (b) spherical model in an infinite soil mass; (c) cylindrical model with
 1062 small values of b_0/a_0 ; (d) spherical model with small values of b_0/a_0 .

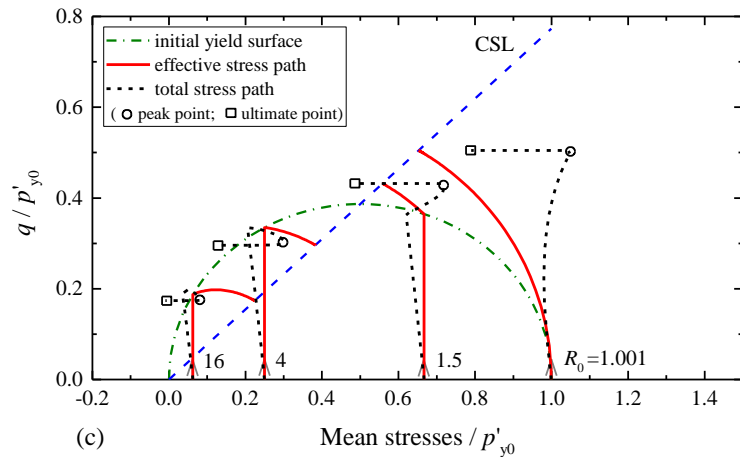
1063



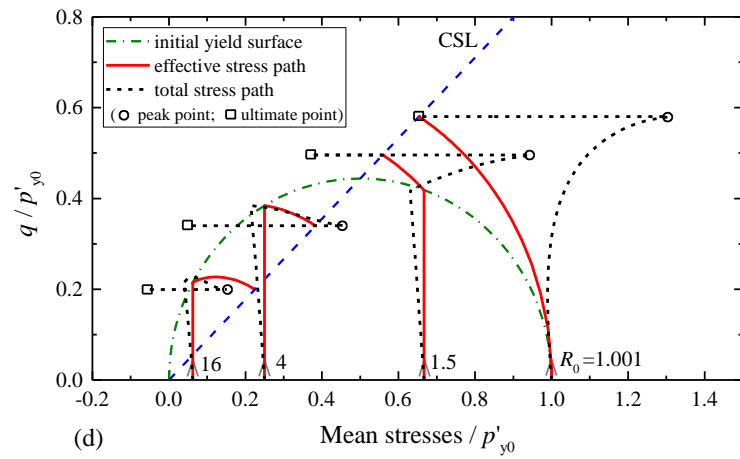
1064



1065



1066



1067

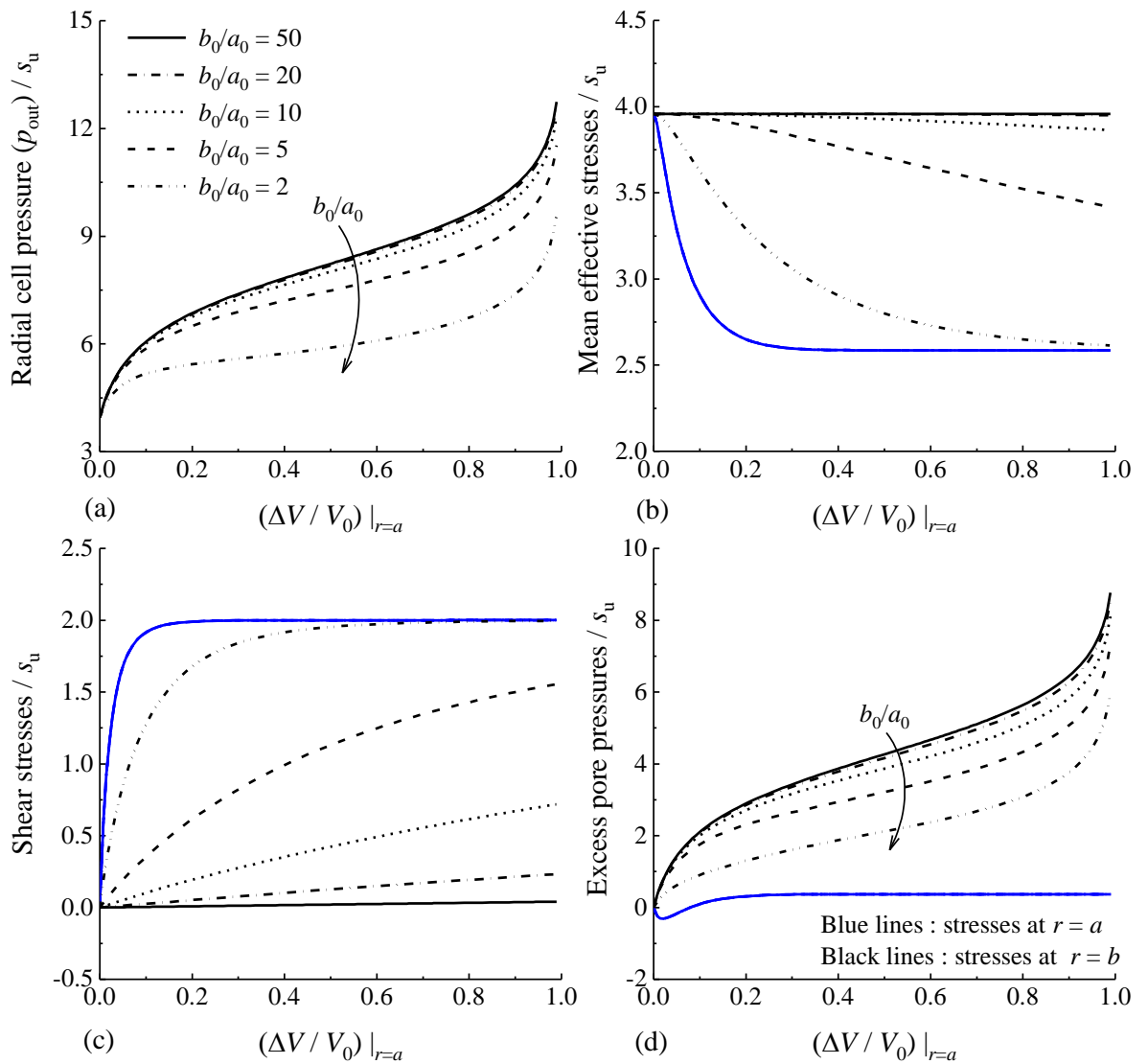
1068

1069

1070

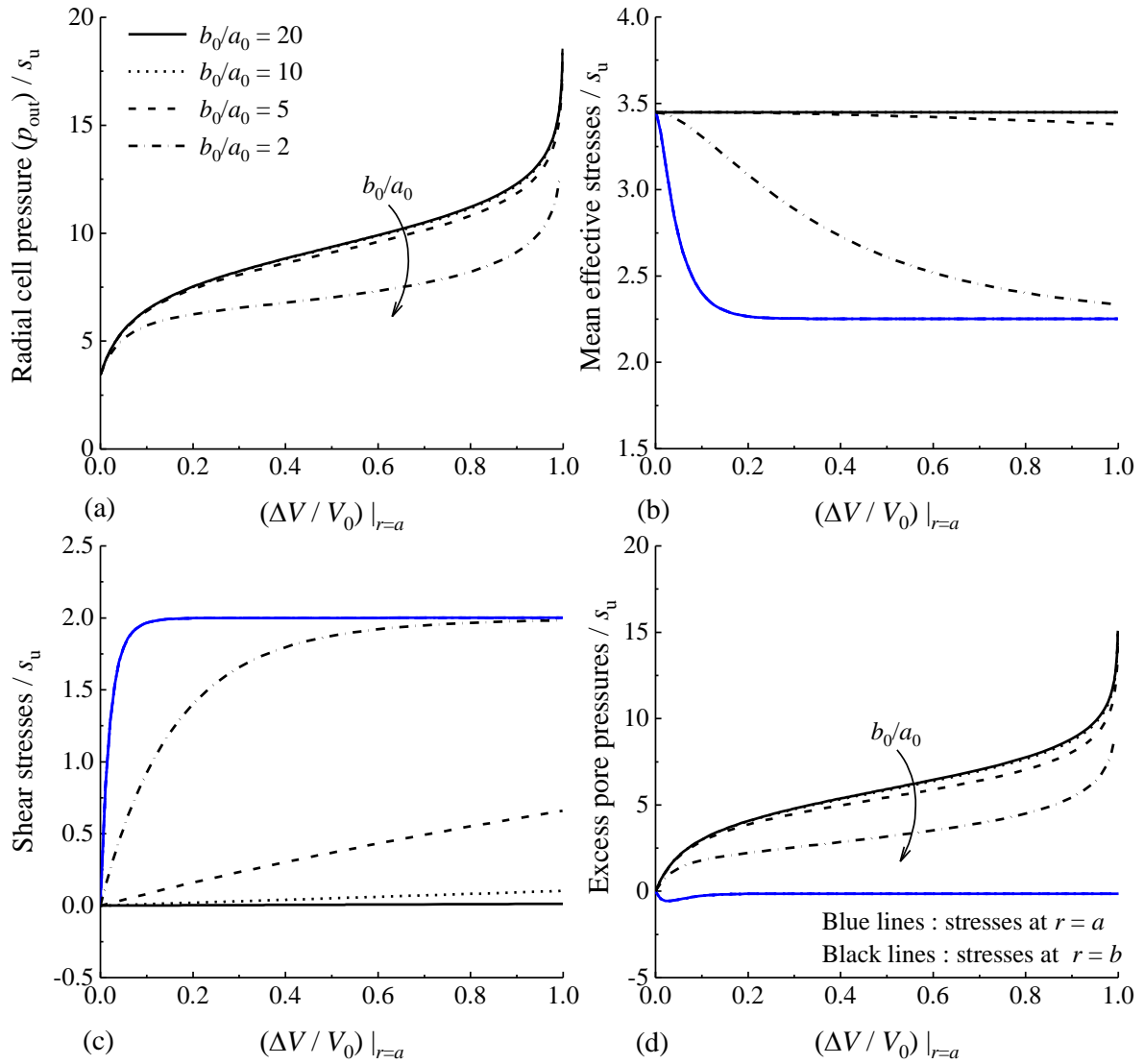
1071

Fig. 6. Typical stress paths in modified Cam clay: (a) cylindrical model with $b_0/a_0=1000$; (b) spherical model with $b_0/a_0=1000$; (c) cylindrical model with $b_0/a_0=2$; (d) spherical model with $b_0/a_0=2$.



1073

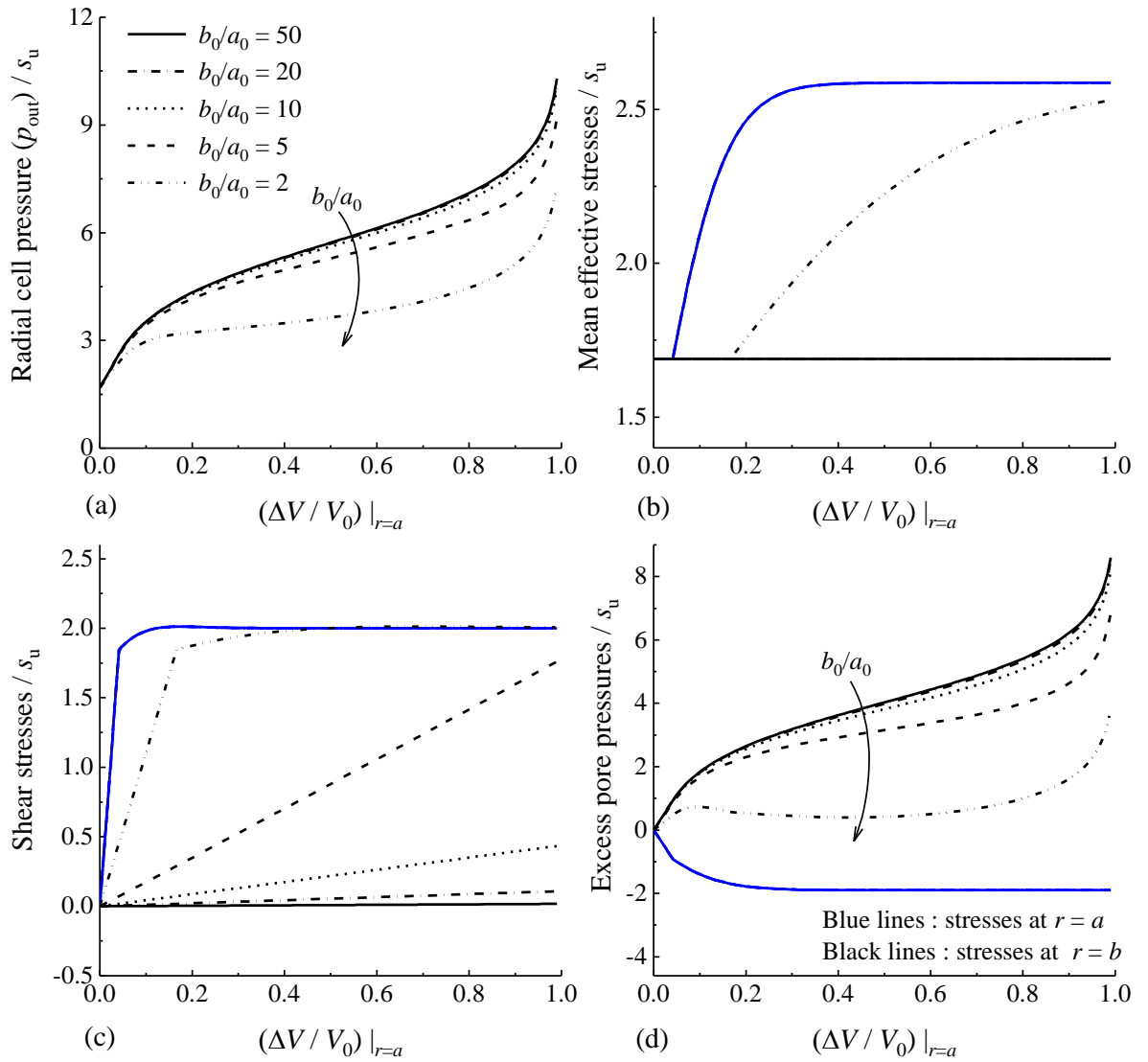
1074 Fig 7. A thick-walled cylinder of normally consolidated London clay ($R_0=1.001$) under
 1075 external loading.



1076

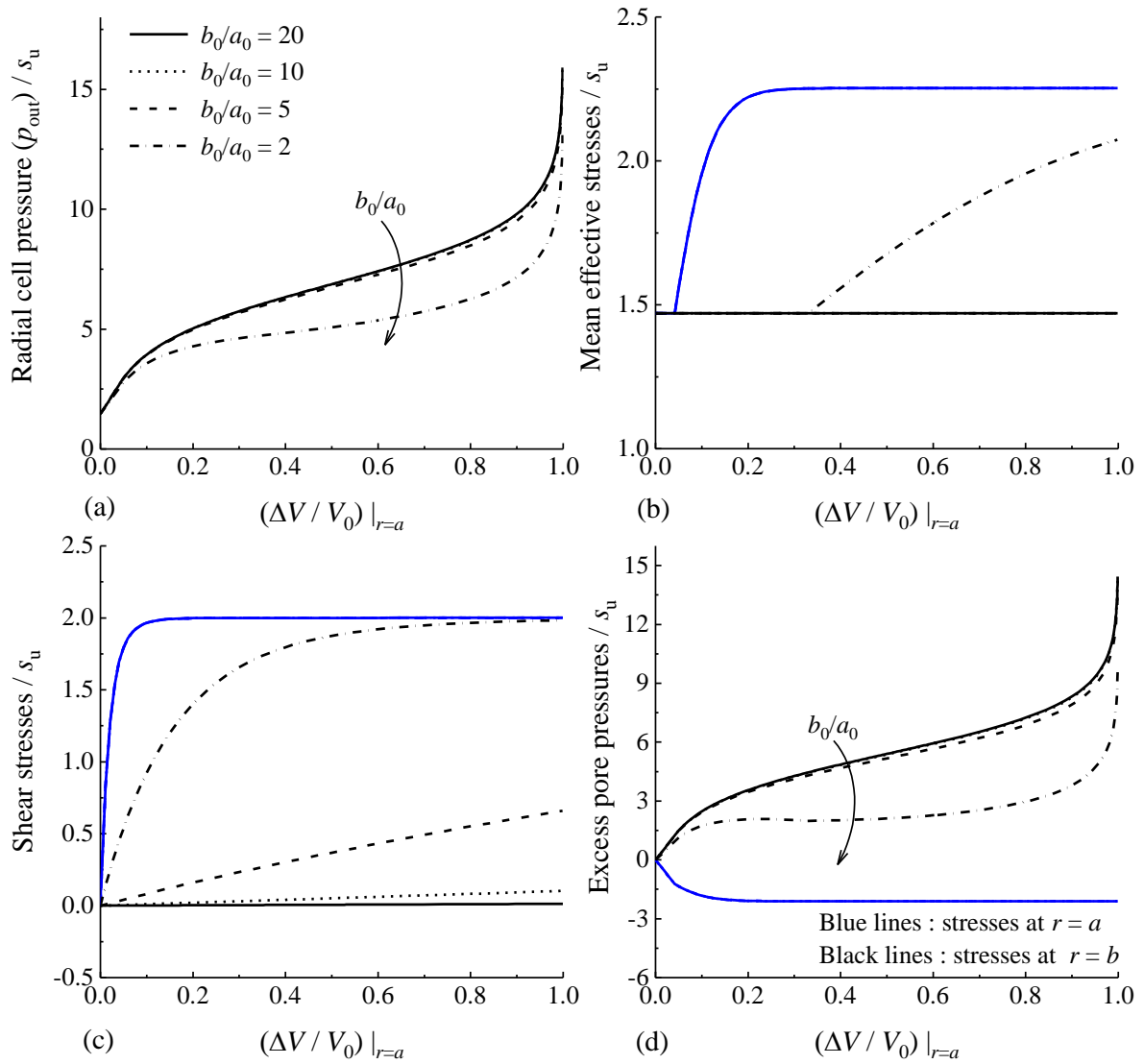
1077 Fig 8. A spherical shell of normally consolidated London clay ($R_0=1.001$) under
 1078 external loading.

1079



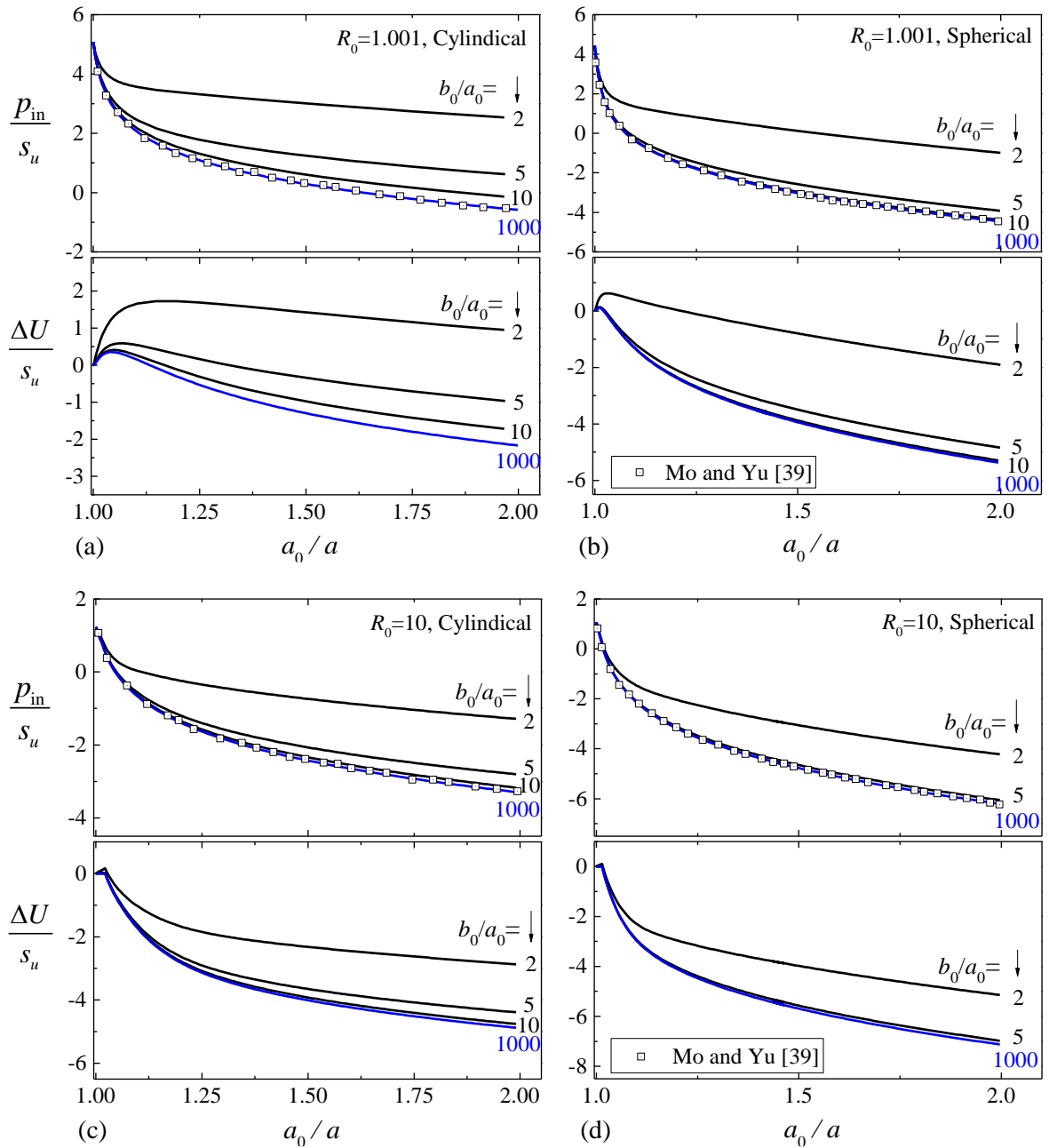
1080

1081 Fig 9. A thick-walled cylinder cavity of stiff London clay ($R_0=4$) under external loading.



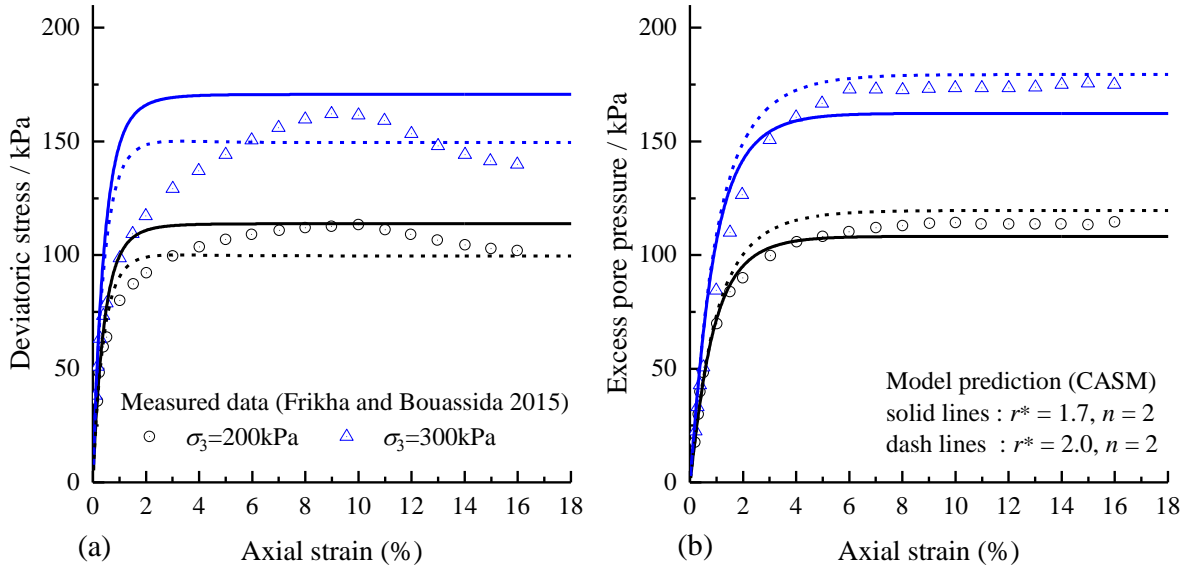
1082

1083 Fig 10. A spherical shell of stiff London clay ($R_0=4$) under external loading.



1086 Fig 11. Cavity contraction curves under internal unloading: (a) and (c) cylindrical
 1087 model; (b) and (d) spherical model.

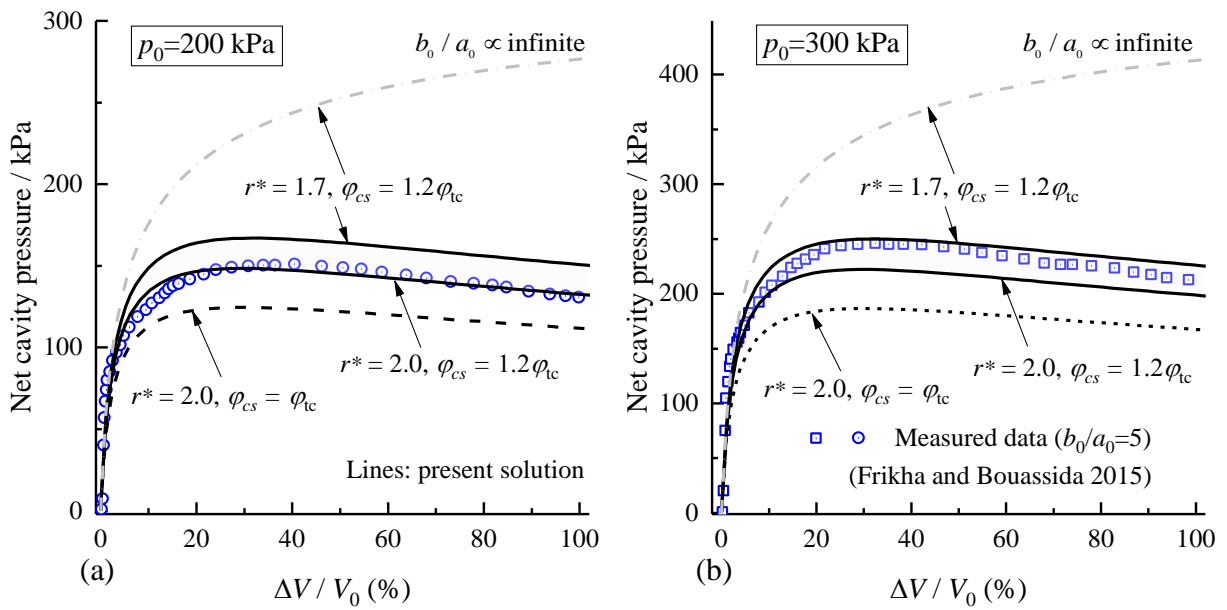
1088



1089

1090 Fig 12. Model prediction for undrained triaxial compression tests with soft Speswhite
1091 kaolin.

1092



1093

1094 Fig 13. Predicted and measured cavity expansion curves in a thick-walled cylinder of
1095 kaolin clay.

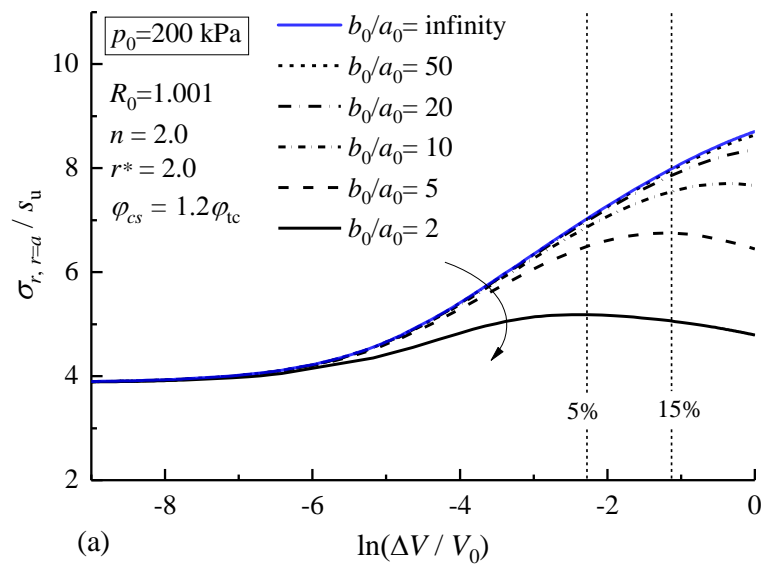
1096

1097

1098

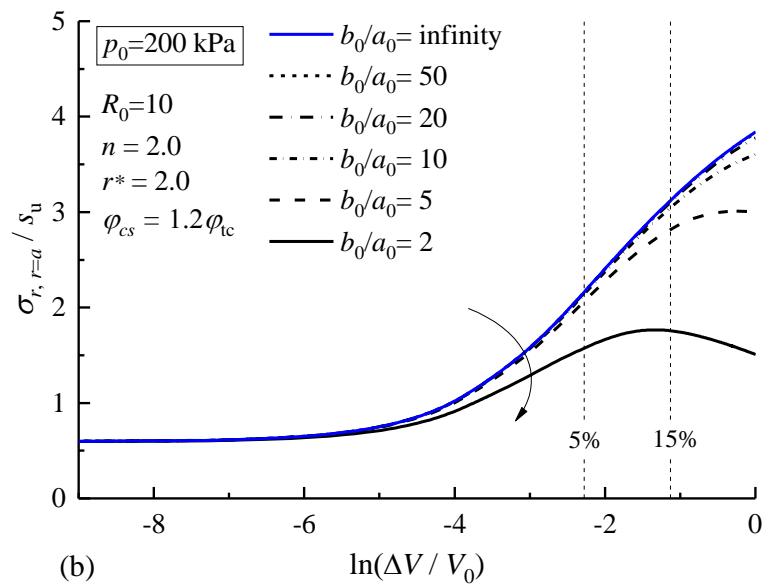
1099

1100



1101

1102



1103

1104 Fig 14. Pressuremeter curves with different values of b_0/a_0 (Speswhite kaolin): (a)

1105 normally consolidated clay ($R_0=1.001$); (b) heavily overconsolidated clay ($R_0=10$).

1106

1107

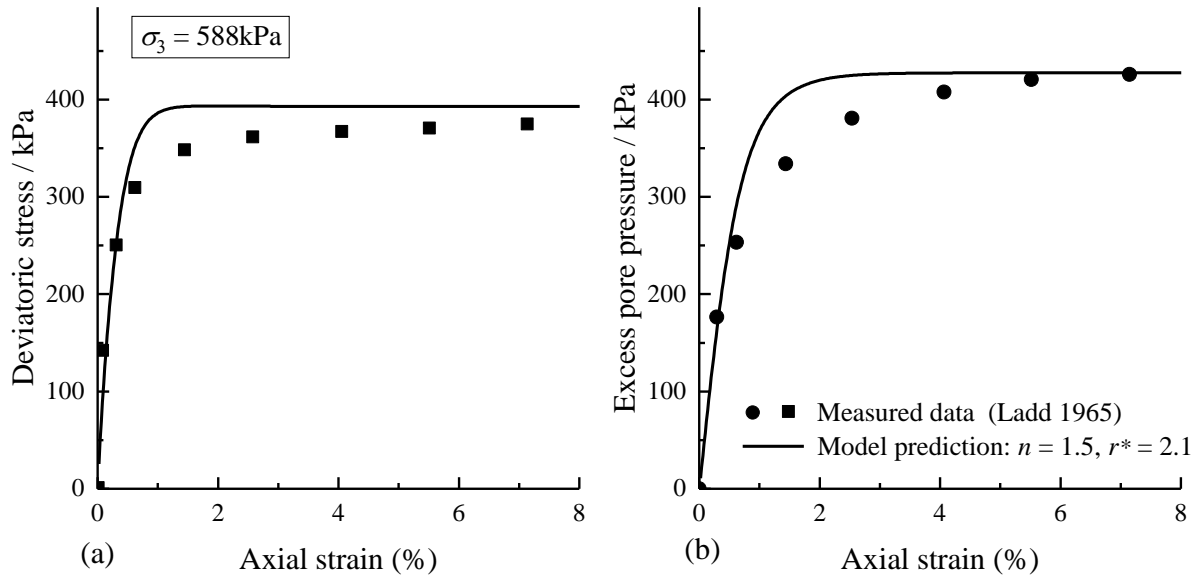
1108

1109

1110

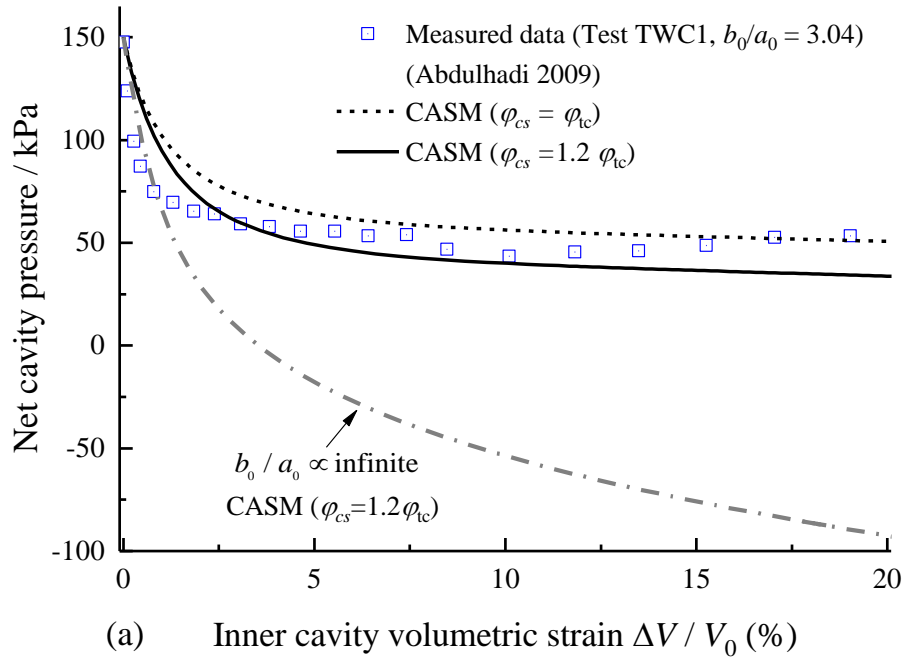
1111

1112
1113
1114



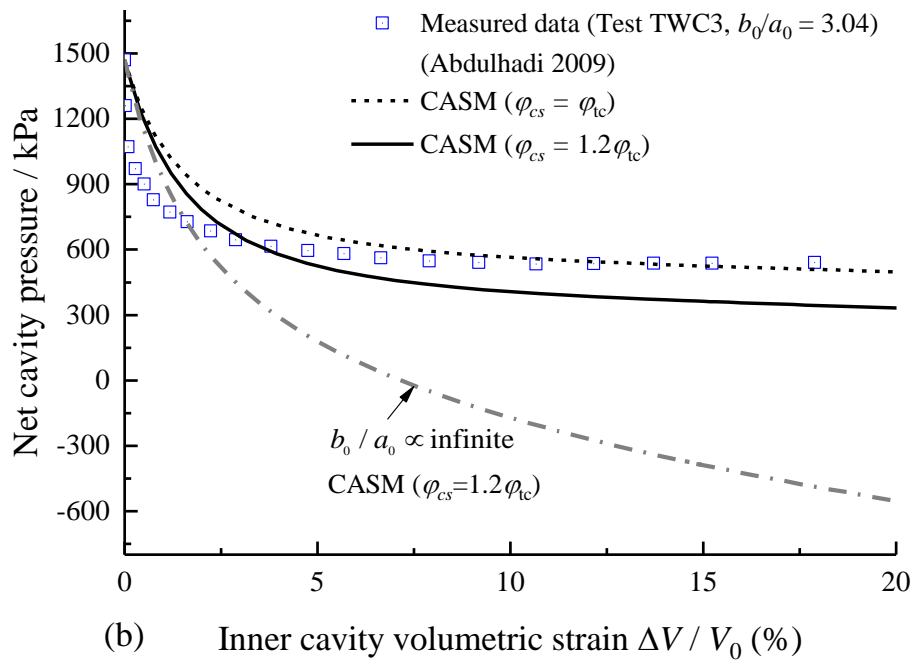
1115
1116
1117
1118
1119
1120
1121
1122
1123

Fig 15. Model prediction for an undrained triaxial compression test on isotropically consolidated RBBC.



1124

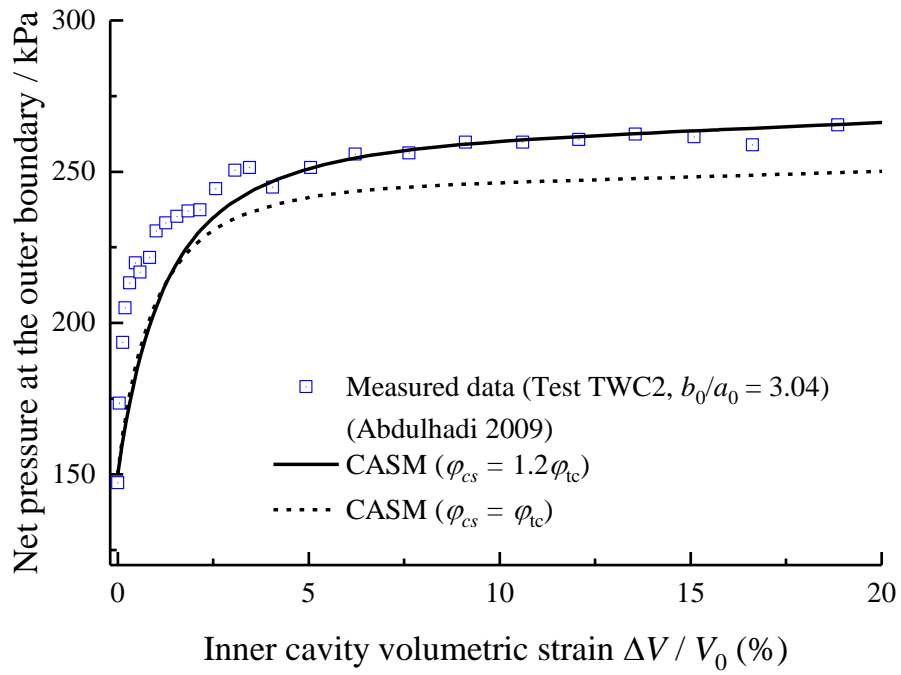
1125



1126

1127 Fig 16. Predicted and measured cavity contraction curves in thick-walled cylinders of
 1128 RBBC under internal unloading.

1129



1130

1131 Fig 17. Predicted and measured cavity contraction curves in a thick-walled cylinder of
 1132 RBBC under external loading.

1133